The Centres of Galaxy Group Dark Matter Halos

The Centres of Galaxy Group Dark Matter Halos

By

Marie-Pier Neault, B.Sc.

A Thesis
Submitted to the School of Graduate Studies
in Partial Fulfilment of the Requirements
for the Degree
Master of Science

McMaster University

MASTER OF SCIENCE (2014) McMaster University

(Department of Physics and Astronomy) Hamilton, Ontario

TITLE: The Centres of Galaxy Group Dark Matter Halos

AUTHOR: Marie-Pier Neault, B.Sc.

SUPERVISOR: Laura Parker

NUMBER OF PAGES: ix, 74

Abstract

Galaxies, galaxy groups and galaxy clusters are embedded in large dark matter halos. Most galaxies in the local universe are found in the galaxy group environment. Locating the centres of galaxy groups is crucial in order to study their properties such as their halo masses. It is often assumed that the most massive galaxy (or brightest galaxy) resides at the centre of the gravitational potential. With the aim of evaluating the validity of this paradigm in galaxy groups, we used two different methods to probe the centres of galaxy group halos: the weak gravitational lensing and dynamical methods. We use these two methods to determine the best definition of galaxy group centres.

Our sample is composed of 49 optically (spectroscopically) selected groups and 36 high quality X-ray-selected groups. In total our sample is composed of 78 distinct groups in the redshift range $0.1 < z < 0.9$ from the GEEC sample. Our weak lensing analysis suggests that the weighted centre is a better definition than the most massive galaxy position. We address the question of whether or not the result is significantly different for X-ray and optically selected systems. For optically selected systems, the weighted centre is a significantly better assumption of the group centre than the most massive galaxies position. For the X-ray selected groups, the weighted centre and the most massive galaxy appear to trace the centre equally well, although the best definition is the location of the peak in X-ray emission. We evaluate, for the first time, the impact of dynamically complex groups on weak lensing analysis. Once we removed dynamically complex systems from our sample, the lensing signals for all centre definitions are in better agreement suggesting that groups with large offsets between the centre definitions are unevolved systems. For the dynamical method, velocity dispersion profiles suffer from large uncertainties and, therefore, we are unable to place any constraint on the centre definition from this technique.

Acknowledgements

I would like to sincerely thank my supervisor Dr. Laura Parker for her rigour and great patience. She has been a demanding supervisor and I have learned so much because of it. I am really proud of my accomplishment which would not have been possible without her.

I would also like to thank Dr. Bill Harris and Dr. James Wadsley, my Master's committee members, for their support and for sharing their time in the completion of this project.

A special thank to Nathan, Rachel, Maximilien and Gwen for investing a lot of their time helping me with corrections of my thesis.

J'aimerais faire un remerciement spécial à ma famille pour leur dévouement et encouragement tout au long de mon parcours scolaire. Sans leur support, je n'aurais jamais pu réaliser une maîtrise en astrophysique en anglais!

Table of Contents

List of Figures

List of Tables

Chapter 1

Introduction

With modern telescope technology we are now capable of observing the distant early universe in unprecedented detail. Numerous observational probes, including studies of the cosmic microwave background, high redshift supernovae and the mapping of large scale structure have led to a new standard model of cosmology, called the Lambda Cold Dark Matter (hereafter ΛCDM) model. According to the ΛCDM paradigm, the Universe is spatially flat, approximately 13.8 billion years old, and is composed, at present, of ordinary matter at 4.9%, dark matter at 26.8%, and of dark energy at 68.3% (Planck Collaboration et al., 2013). Ordinary matter, also referred to as baryonic matter, consists of all matter in the Universe composed of protons and neutrons[1]. These two components together form atomic nuclei and hence atoms which make up all of the visible matter in the Universe.

Dark Matter (hereafter DM) is a proposed type of matter, which can explain numerous gravitational effects observed on visible matter. The existence of DM was first proposed by Fritz Zwicky in the 1930s to explain the dynamics of galaxies in the Coma cluster. Further evidence for the existence of DM came in the 1970's with the observation of the flat rotation curves in the Andromeda and other nearby galaxies (e.g. Rubin et al., 1962). These two important observations provided the first compelling evidence for the existence of dark matter. Using these and other techniques there is now compelling evidence that galaxies are embedded in large dark matter halos. Observational evidence of dark matter is discussed in further detail in Section 1.1. In this thesis, we adopt the ΛCDM model as described in Section 1.1.1.

---

[1] Neglecting the small mass contribution of leptons

Dark Energy (hereafter DE) is a vacuum energy component proposed to explain the accelerated expansion of the Universe. This repulsive force was first confirmed in 1998 through the analysis of the photometric observations of distant supernovae as a function of redshift (Riess et al., 1998; Perlmutter et al., 1999). Other evidence supporting the existence of DE is the anisotropy in the temperature fluctuations of the CMB. The best fit to the angular power spectrum of the CMB fluctuations indicates that the Universe is spatially close to flat. However, baryonic and dark matter represent together only 30% of the critical density of the Universe for closure (de Bernardis et al., 2000; Spergel et al., 2007; Komatsu et al., 2011; Planck Collaboration et al., 2013), implying that 70% of the composition of the Universe is missing which is consistent with the result from Riess et al. (1998) and Perlmutter et al. (1999). Other observations such as the growth of large-scale structure (e.g. Linder & Jenkins, 2003), the late-time integrated Sachs-Wolfe effect (Boughn & Crittenden, 2004), baryon acoustic oscillations (BAO) (Percival et al., 2010; Beutler et al., 2011) and weak lensing detection at large scales (e.g. Massey et al., 2007; Semboloni et al., 2011) also support the existence of DE. The cosmological constant Λ, is a proposed model to DE where the energy density is constant in contrast to alternative models with a time varying density of vacuum energy. All present observational results are consistent with a Λ model of DE, which is the model adopted in this thesis.

The composition of the Universe plays an important role in its evolution. At large scales, the distribution of the structure into walls, voids, and filaments, depends critically on the abundance of DM and DE. On smaller scales, the effect of cosmic expansion is negligible and the evolution of a galaxy is mostly related to its host dark matter halo (through its environment) and to its baryonic matter (through its stellar mass, history, feedback, etc). As dark matter is not visible at any wavelength, it cannot be observed directly. Consequently, the properties of dark matter halos enveloping galaxies, groups, and clusters must be observed indirectly by detecting their influence on the luminous matter we do see. In this work, we study a relatively understudied topic in modern extragalactic astronomy: the mass distribution of dark matter halos in galaxy groups.

Various techniques to measure DM halo masses exist, such as satellite kinematics, strong gravitational lensing and weak gravitational lensing. However, these techniques are sensitive to the choice of centering. The aim of this thesis is to apply these techniques using different centre definitions in order to identify which definition best trace the real centre in groups. Two of the previously mentioned methods are involved in this work. The *weak gravitational lensing method* consists of a statistical measurement of the tangential component of background galaxy shapes (see Section 2.2) and the *dynamical method* requires visible tracers such as satellites to measure the velocity dispersion (see Section 2.3).

From the standard picture of galaxy formation, it is often assumed that the most massive galaxy resides at rest in the central potential, particularly in evolved groups (van den Bosch et al., 2005). This paradigm stems from the fact that the dynamical friction effect in high density systems slows down the most massive galaxies. The loss of angular momentum tends to cause the massive galaxies to segregate towards the halo potential centre. This model is referred as the central galaxy paradigm (hereafter CGP, van den Bosch et al., 2005). Dynamical friction timecales are typically long but massive galaxies with small offsets will sink to the centre of the potential relatively quickly. The central galaxy will accrete gas and possibly cannibalize some satellite galaxies and eventually become the most massive galaxy of the system. We provide an initial investigation of how justified it is to use the most massive galaxy as the centre of mass in galaxy groups. In particular, we investigate whether or not, using the galaxies' mass weighted centre as the centre of the group is a better assumption for tracing the DM halo mass profile.

1.1 Dark Matter Halos

Evidence for the existence of dark matter first emerged in the 1930s with Zwicky's observations of the motion of galaxies in the Coma galaxy cluster. Using the virial theorem to infer the mass of the cluster, Zwicky calculated the velocity dispersion from the radial velocities of galaxies within the cluster. From the comparison of the luminosity to the virial mass of the cluster, he realized that the mass-to-light ratio was higher than his expectation by a factor of $\sim 10^2$

indicating the presence of large amounts of unseen matter (Zwicky, 1937). Further evidence of dark matter came in the 1960s and 1970s with a careful examination of the rotation curve of the Andromeda galaxy by Rubin Vera and collaborators (Rubin & Ford, 1970). Assuming that mass traces light, Kepler's third law predicts that the velocity should decrease as a function of the distance from the nucleus. However, Rubin's observations revealed a flat extended galaxy rotation curve for Andromeda. Attempts to explain the discrepancy between the rotational motion predicted based on the luminous matter and the observations led to strong evidence for the existence of dark matter.

In addition to optical rotation curves, evidence of extended dark matter halos comes from the measurements of the Doppler shift of the 21 cm line (radio) of neutral hydrogen (HI) (Roberts & Rots, 1973; Bosma, 1978; van Albada et al., 1985). Albert Bosma first demonstrated that the rotation curve was roughly constant at large galactocentric distances in multiple spiral galaxies, providing the first evidence that dark matter halos surrounding galaxies were not just observed in one or two isolated cases but were present in many spiral galaxies (Bosma, 1978). This method also provided the first evidence that galaxies are embedded in large and massive DM halos where HI regions were detected out to 30-50 kpc, which far exceeds the optical extent of galaxies (Ostriker et al., 1974; Faber & Gallagher, 1979; Sancisi & van Albada, 1987; Sofue & Rubin, 2001). Later studies using satellite dynamics (Zaritsky et al., 1993; Zaritsky & White, 1994) and the weak lensing method (e.g. Fischer et al., 2000) confirmed the presence of DM halos out to ∼200-400 kpc.

1.1.1 CDM model

There is now overwhelming evidence that DM represents roughly 85% of the total matter in the Universe, where the other 15% is ordinary matter (Komatsu et al., 2011; Planck Collaboration et al., 2013a). The known properties of this mysterious matter are that it only interacts with gravity, it has a very weak or no interaction with electromagnetic radiation and weak or no interaction with itself. At the present day, a strong candidate for the hypothetical form of dark matter is Cold Dark Matter (hereafter CDM). CDM particles move non-relativistically which allows them to clump efficiently and differentiates them from competing theories: the warm and hot dark matter particles. While it was first proposed in the early 1960's that galaxy structures formed by fragmentation, referred to as the *top-down* scenario (Eggen et al., 1962), it has now been shown that the growth of large-scale structure is hierarchical in nature as proposed in the Searle & Zinn (1978) model. From collapsing and merging of small systems under their own self-gravity, larger systems are created and eventually form the largest structures we observe today. This model, also referred to as the *bottom-up* scenario, has been supported by multiple observational and simulation studies (e.g. Press & Schechter, 1974; Lacey & Cole, 1993; Springel et al., 2005). This structure formation model requires a slow hypothetical dark matter particle which would not be able to escape the gravitational potential of the primordial mass fluctuations. Therefore, measuring the distribution of mass in the Universe provides the opportunity to test the CDM model and address one of the most intriguing questions in modern astronomy: what is the nature of dark matter? The properties of DM can be determined through the analysis of DM halo sizes, shapes and density profiles.

1.1.2 Dark Matter Halo density profile

In order to extract physical properties of dark matter halos, such as the halo size, the velocity dispersion and hence the dynamical mass, the observations need to be fit by an assumed halo mass model. The most common observational model to fit DM halo density profiles is the singular isothermal sphere (hereafter SIS) used for its simplicity.

The SIS profile is given by the following density distribution (Binney & Tremaine, 1987):

$$\rho_{SIS}(r) = \frac{\sigma^2}{2\pi G r^2} \tag{1.1}$$

where σ is the velocity dispersion, G is the universal gravitational constant and r is the distance from the centre assuming a spherically isotropic density profile. By integrating the mass up to the virial radius defined as R_{200} (as defined is Section 3.4), one would get the following relation:

$$M_{SIS} = \frac{2\sigma^2 R_{200}}{G} \tag{1.2}$$

Hence from the estimation of the velocity dispersion of the group, it becomes possible to evaluate the mass profile of the dark matter halo. This simple profile is convenient because its density profile ($\rho \propto r^{-2}$) is consistent with the observed flattened velocity profile.

Other than the differences in their mass, dark matter density profiles around galaxies, groups and clusters in simulation are remarkably similar (Dubinski & Carlberg, 1991; Navarro et al., 1995). The investigation, made by Navarro et al. (1995, 1996, 1997) developed a density profile for dark matter halos that culminated in the realization of the Navarro-Frenk-White (hereafter NFW) density profile. This universal density profile consists of a broken power law that traces a density profile as $\rho \propto r^{-1}$ towards the centre, $\rho \propto r^{-3}$ in the outer regions and, in the intermediate region, the density profile can look like $\rho \propto r^{-2}$. This profile can be applied to a large range of objects from individual galaxies up to galaxy clusters. This spherically averaged density profile is given by a two-parameter equation:

$$\rho_{NFW}(r) = \frac{\delta_c \rho_c}{(r/r_s)(1 + r/r_s)^2} \tag{1.3}$$

where r is the distance from the centre. The critical density for the closure of the Universe (ρ_c) is defined as $\rho_c(z) = [3H^2(z)]/(8\pi G)$, where G in the universal gravitational constant, and $H(z) = H_0\sqrt{\Omega_M(1+z)^3 + \Omega_\Lambda}$ is the Hubble constant at redshift z, H_0 is the Hubble constant today, and Ω_M and Ω_Λ are the DM and DE density relative to the density of a critical-density Universe respectively. The characteristic overdensity (δ_c) which is defined as $\delta_c = 200c^3/[3\ln(1+c) - c/(1+c)]$, and the scale radius, which is defined as $r_s = R_{200}/c$ are dependent on the two free parameters c which is a dimensionless number known as the concentration parameter, and R_{200} which is defined as the virial radius (see Section 3.4 for more details). The integrated mass inside the virial radius using the NFW density profile gives:

$$M_{NFW} = \frac{800\pi}{3}\rho_c R_{200}^3 \tag{1.4}$$

Hence the dark matter mass distribution can be extracted from the estimation of R_{200}. Observational studies of dynamics, gravitational lensing, X-ray clusters and galaxy group properties are broadly consistent with the NFW profile (Prada et al., 2003; Pointecouteau et al., 2005; Comerford et al., 2006; Mandelbaum et al., 2006b). The SIS is often adopted rather than the NFW since the NFW has an extra free parameter. It has been stressed in Wright & Brainerd (2000) that the SIS tends to overestimate the total mass compared to the NFW. In this work, as will be presented in future chapters, we are interested in a relative profiles between different samples hence the differences between these mass models are not important.

1.2 Galaxy Groups

Galaxy groups are typically defined as consisting of 2 to 50 galaxy members which are gravitationally bound to one another and orbit around a given centre. This definition is somewhat arbitrary, but systems with less than three members are more likely to have projection issues and systems with more than 50 galaxies are typically galaxy clusters as, in observational studies of distant systems, we only observe the brightest group members, and many faint members fall below our detection limit. Groups of galaxies represent the most common environment in the Universe composing no less than 50% of the galaxy population at the present day (Geller & Huchra, 1983; Eke et al., 2005).

Even though galaxy groups play an important role in the formation of large scale structure and widely affect the properties of galaxies, detailed studies of galaxy groups and their evolution are still limited in comparison to studies of field galaxies and clusters. This is mainly due to the fact that groups are difficult to identify in comparison to galaxy clusters which are easy to identify by their huge over density of red galaxies or their bright X-ray emission. For this reason most galaxy group studies have been restricted to galaxy groups which are either compact

Table 1.1: Lists of Groups Catalogues

Group catalog	Survey	Redshift Range	Number of Groups	Halo Mass ($M_\odot$)	Algorithm Finder
Eke et al. (2004)	2dFGRS	$0 < z < 0.3$	>7000	$\sim 10^{11.5} - 10^{15.5}$	F-O-F
Yang et al. (2007)	SDSS	$0.01 < z < 0.2$	>5000	$10^{12.5} - 10^{15}$	halo-based
Carlberg et al. (2001)	CNOC2	$0.1 < z < 0.6$	>~200	$\sim (10^{12} - 10^{15})^a$	F-O-F
Wilman et al. (2005)	GEEC	$0.1 < z < 0.85$	>70	$\sim 10^{12} - 5 \times 10^{14}$	F-O-F
Knobel et al. (2009)	zCOSMOS	$0.1 < z < 1$	102	$10^{12.5} - 10^{14.5}$	F-O-F
Gerke et al. (2005)	DEEP2	$0.6 < z < 1.3$	1295	$\sim (10^{12} - 10^{15})^a$	VDM

---

[a] The mass range has been estimated from the velocity dispersion range

(Hickson et al., 1989) or X-ray luminous (Mulchaey et al., 2003). However, from large field galaxy surveys with high spectroscopic completeness it has become possible to detect galaxy groups via sophisticated algorithms such as the Friends-of-Friends algorithm (F-O-F, Huchra & Geller, 1982), the Voronoi-Delaunay algorithm (VDM, Marinoni et al., 2002), and the Halo-based group finder algorithm (Yang et al., 2005a) which are based on the three dimensional galaxy density. There are now relatively large group samples based on these algorithms such as: the Canadian Network for Observational Cosmology (CNOC2) galaxy redshift survey catalog (Carlberg et al., 2001) which later evolved to the Group Environment Evolution Collaboration (GEEC, Wilman et al., 2005; Connelly et al., 2012), Two-degree Field Galaxy Redshift Survey (2dFGRS, Eke et al., 2005), the second Deep Extragalactic Evolutionary Probe (DEEP2, Gerke et al., 2005), Sloan Digital Sky Survey Data Release 4 (SDSS DR4, Yang et al., 2007), and Cosmic Evaluation Survey (zCOSMOS, Knobel et al., 2009). A detailed list of these catalogs is given in Table 1.2.

1.3 Galaxy Group Centres

The centres of galaxy clusters and groups can be defined as the mass centroid, most bound particle or density peak. The disparity between these centre definitions is caused by asphericity or substructure in the system. Techniques such as strong gravitational lensing, weak gravitational lensing and dynamical methods require an assumption about the location of the halo centre. The misidentification of the centre may over- or underestimate the velocity dispersion, the mass and the size of the systems, or result in a misidentification of the dynamical state of the system. Therefore, locating the centre of the potential in groups and clusters represents an important step in order to extract their properties. Observationally, the centre definition in groups and clusters is restricted to the available measurements such as the X-ray emission and the luminosity of their galaxy members. Therefore, galaxy cluster centres are often defined as the peak of radiating hot gas (e.g. Lin et al., 2004) or the position of the brightest halo galaxy (hereafter BHG, Johnston et al., 2007; Umetsu et al., 2014). As the location of the BHG is mostly consistent with the location of the peak of X-ray emission, the choice of centering in clusters is usually not a concern (e.g. Johnston et al., 2007). Although, investigations in clusters have demonstrated that some BHGs may lie significantly far from the local density peaks (e.g. von der Linden et al., 2007; Hwang & Lee, 2008) or may not be located at the bottom of the potential well (e.g. Beers & Geller, 1983; Oegerle & Hill, 2001; Coziol et al., 2009).

The centres of galaxy groups are not as straightforward to identify as the centres of clusters. This largely stems from the fact that not all groups are detected in deep X-ray imaging. Hence, the centre's definition in groups cannot be based on the X-ray emission alone. On the other hand, using the BHG as the centre in groups may be problematic as the BHGs may not be located at the centre of the system if the group is in process of forming or not fully in equilibrium. From the CGP models, it is reasonable to assume that the brightest or most massive galaxy resides at rest at the centre of the system if the system is sufficiently evolved. As groups of galaxies span a wide range of dynamical states, from just forming to fully virialized (Zabludoff & Mulchaey, 1998; Rasmussen et al., 2006), it is not safe to assume that BHGs reside at their centre. Additionally, groups have fewer members as compared clusters, hence small perturbations present stronger effects on the equilibrium of the system. Recent studies on the dynamical state in groups have identified a significant fraction of young or complex groups in the GEEC, 2dFGRS and SDSS catalog (Hou et al., 2009; Ribeiro et al., 2010; Martínez & Zandivarez, 2012).

While the CGP is an assumption that has been used by many authors in the aim of measuring halos masses (e.g. McKay et al., 2002; Prada et al., 2003; van den Bosch et al., 2004; More et al., 2009; Mandelbaum et al., 2006a; Johnston et al., 2007), there are now multiple studies proposing that the BHGs are not necessary the central galaxy. van den Bosch et al. (2005) showed that BHGs which reside in groups with halo mass larger than $10^{13}h^{-1}\mathrm{M}_\odot$ have non-zero value for their velocity which was later supported by Skibba et al. (2011). From the SDSS galaxy group catalog, Skibba et al. examined the statistic R which is the offset of the line-of-sight velocities of the brightest group galaxies relative to the group satellites, as well as S the projected position offset. Then, they compared these cumulative distributions with those obtained from detailed mock groups catalogs where (1) the central galaxy is the brightest object and is at rest at the centre of the potential well, (2) the central galaxy is the brightest galaxy but has a spatial offset with respect to the halo potential well centre and (3) the central galaxy is not the brightest galaxy but resides at rest at the centre of the potential well. Their statistical results suggest that the central galaxy is not the brightest galaxy in a non-negligible fraction of systems and may have an offset with the potential well centre. Furthermore, Skibba et al. also found that the fraction of halos in which the brightest galaxy is not the central one is increasing as a function of the halo mass. One possible explanation of this observation is the presence of substructure in the dark matter halos.

In contrast to these findings, George et al. (2012) compared different centre definitions using the weak lensing method for a sample of 129 X-ray galaxy groups from the COSMOS survey. Their results suggest that the brightest or the most massive galaxy appears to be the best tracer of the centre of mass of halos as compared to centroid definitions such as the X-ray luminosity density peak. The contradiction between these two results may be caused by misidentification of the most massive galaxy. Two major factors responsible for the misidentification of the most massive galaxy are the redshift incompleteness and the uncertainty on the luminosity and hence the stellar mass. This issue is taken into account on our sample in Section 3.3

1.4 Thesis Objectives

The main goal of this thesis is to explore different definitions of galaxy group centres to try and ascertain which one best represents the true centre of the group potential. Two different candidate centres are compared: the galaxies' mass weighted centre and the most massive galaxy location. This analysis provides the opportunity to evaluate the validity of the CGP. The techniques used in order to identify the best centre definition are the weak lensing method and a dynamical method. The observational data used in this thesis comes from the Group Environment and Evolution Collaboration (GEEC) survey. This work begins with a more technical description of the methodology including weak gravitational lensing and the dynamical method in Chapter 2. A description of the data and the different candidate centres used in this work can be found in Chapter 3. In Chapter 4, we show weak lensing and dynamics results. In Chapter 5, we conclude with possible interpretations and a discussion of our results.

Bibliography

Beers, T. C., & Geller, M. J. 1983, ApJ, 274, 491

Bekenstein, J. D. 2004, Phys. Rev. D, 70, 083509

Beutler, F., Blake, C., Colless, M., et al. 2011, MNRAS, 416, 3017

Binney, J., & Tremaine, S. 1987, Princeton, NJ, Princeton University Press, 1987, 747 p.,

Bosma, A. 1978, Ph.D. Thesis,

Boughn, S., & Crittenden, R. 2004, Nature, 427, 45

Brainerd, T. G., & Wright, C. O. 2000, arXiv:astro-ph/0006281
L25

Carlberg, R. G., Yee, H. K. C., Morris, S. L., et al. 2001, ApJ, 552, 427

Clowe, D., Bradač, M., Gonzalez, A. H., et al. 2006, ApJ, 648, L109

Comerford, J. M., Meneghetti, M., Bartelmann, M., & Schirmer, M. 2006, ApJ, 642, 39

Connelly, J. L., Wilman, D. J., Finoguenov, A., et al. 2012, ApJ, 756, 139

Coziol, R., Andernach, H., Caretta, C. A., Alamo-Martínez, K. A., & Tago, E. 2009, AJ, 137, 4795

Davé, R., Spergel, D. N., Steinhardt, P. J., & Wandelt, B. D. 2001, ApJ, 547, 574

de Bernardis, P., Ade, P. A. R., Bock, J. J., et al. 2000, Nature, 404, 955

Dubinski, J., & Carlberg, R. G. 1991, ApJ, 378, 496

Eggen, O. J., Lynden-Bell, D., & Sandage, A. R. 1962, ApJ, 136, 748

Einasto, J., Kaasik, A., & Saar, E. 1974, Nature, 250, 309

Eke, V. R., Baugh, C. M., Cole, S., et al. 2004, MNRAS, 348, 866

Eke, V. R., Baugh, C. M., Cole, S., et al. 2005, MNRAS, 362, 1233

Faber, S. M., & Gallagher, J. S. 1979, ARA&A, 17, 135

Famaey, B., & McGaugh, S. S. 2012, Living Reviews in Relativity, 15, 10

Fischer, P., McKay, T. A., Sheldon, E., et al. 2000, AJ, 120, 1198

Fitchett, M. J. 1988, The Minnesota lectures on Clusters of Galaxies and Large-Scale Structure, 5, 143

Geller, M. J., & Huchra, J. P. 1983, ApJS, 52, 61 J. A., Davis, M., et al. 2005, ApJ, 625, 6

Gerke, B. F., Newman, J. A., Davis, M., et al. 2005, ApJ, 625, 6

George, M. R., Leauthaud, A., Bundy, K., et al. 2012, ApJ, 757, 2

Hickson, P., Kindl, E., & Auman, J. R. 1989, ApJS, 70, 687

Hoekstra, H., Franx, M., Kuijken, K., et al. 2001, ApJ, 548, L5

Hoekstra, H., Yee, H. K. C., & Gladders, M. D. 2004, ApJ, 606, 67

Hou, A., Parker, L. C., Harris, W. E., & Wilman, D. J. 2009, ApJ, 702, 1199

Huchra, J. P., & Geller, M. J. 1982, ApJ, 257, 423

Hwang, H. S., & Lee, M. G. 2008, ApJ, 676, 218

Johnston, D. E., Sheldon, E. S., Wechsler, R. H., et al. 2007, arXiv:0709.1159

Kaiser, N., & Squires, G. 1993, ApJ, 404, 441

Kaiser, N., Squires, G., & Broadhurst, T. 1995, ApJ, 449, 460

Kawata, D., & Mulchaey, J. S. 2008, ApJ, 672, L103

Komatsu, E., Smith, K. M., Dunkley, J., et al. 2011, ApJS, 192, 18

Knobel, C., Lilly, S. J., Iovino, A., et al. 2009, ApJ, 697, 1842

Lacey, C., & Cole, S. 1993, Observational Cosmology, 51, 192

Lin, Y.-T., Mohr, J. J., & Stanford, S. A. 2004, ApJ, 610, 745

Linder, E. V., & Jenkins, A. 2003, MNRAS, 346, 573

Mandelbaum, R., Seljak, U., Kauffmann, G., Hirata, C. M., & Brinkmann, J. 2006a, MNRAS, 368, 715

Mandelbaum, R., Seljak, U., Cool, R. J., et al. 2006b, MNRAS, 372, 758

Mandelbaum, R., Hirata, C. M., Broderick, T., Seljak, U., & Brinkmann, J. 2006c, MNRAS, 370, 1008

Marinoni, C., Davis, M., Newman, J. A., & Coil, A. L. 2002, ApJ, 580, 122

Martínez, H. J., & Zandivarez, A. 2012, MNRAS, 419, L24

Massey, R., Rhodes, J., Leauthaud, A., et al. 2007, ApJS, 172, 239

McCarthy, I. G., Frenk, C. S., Font, A. S., et al. 2008, MNRAS, 383, 593

McKay, T. A., Sheldon, E. S., Johnston, D., et al. 2002, ApJ, 571, L85

Milgrom, M. 1983, ApJ, 270, 365

Miralda-Escude, J. 1991, ApJ, 370, 1

More, S., van den Bosch, F. C., Cacciato, M., et al. 2009, MNRAS, 392, 801

Mulchaey, J. S., Davis, D. S., Mushotzky, R. F., & Burstein, D. 2003, ApJS, 145, 39

Navarro, J. F., Frenk, C. S., & White, S. D. M. 1995, MNRAS, 275, 56

Navarro, J. F., Frenk, C. S., & White, S. D. M. 1996, ApJ, 462, 563

Navarro, J. F., Frenk, C. S., & White, S. D. M. 1997, ApJ, 490, 493

Oegerle, W. R., & Hill, J. M. 2001, AJ, 122, 2858

Ostriker, J. P., Peebles, P. J. E., & Yahil, A. 1974, ApJ, 193, L1

Parker, L. C., Hoekstra, H., Hudson, M. J., van Waerbeke, L., & Mellier, Y. 2007, ApJ, 669, 21

Percival, W. J., Reid, B. A., Eisenstein, D. J., et al. 2010, MNRAS, 401, 2148

Perlmutter, S., Aldering, G., Goldhaber, G., et al. 1999, ApJ, 517, 565

Planck Collaboration, Ade, P. A. R., Aghanim, N., et al. 2013a, arXiv:1303.5062

Planck Collaboration, Ade, P. A. R., Aghanim, N., et al. 2013, arXiv:1303.5076

Pointecouteau, E., Arnaud, M., & Pratt, G. W. 2005, A&A, 435, 1

Prada, F., Vitvitska, M., Klypin, A., et al. 2003, ApJ, 598, 260

Press, W. H., & Schechter, P. 1974, ApJ, 187, 425

Rasmussen, J., Ponman, T. J., Mulchaey, J. S., Miles, T. A., & Raychaudhury, S. 2006, MNRAS, 373, 653

Ribeiro, A. L. B., Lopes, P. A. A., & Trevisan, M. 2010, MNRAS, 409, L124

Riess, A. G., Filippenko, A. V., Challis, P., et al. 1998, AJ, 116, 1009

Roberts, M. S., & Rots, A. H. 1973, A&A, 26, 483

Rubin, V. C., Burley, J., Kiasatpoor, A., et al. 1962, AJ, 67, 491

Rubin, V. C., & Ford, W. K., Jr. 1970, ApJ, 159, 379

Rubin, V. C., Thonnard, N., & Ford, W. K., Jr. 1978, ApJ, 225, L107

Sancisi, R., & van Albada, T. S. 1987, Dark matter in the universe, 117, 67

Sanders, R. H. 1990, A&A Rev., 2, 1

Schneider, P., & Rix, H.-W. 1997, ApJ, 474, 25

Searle, L., & Zinn, R. 1978, ApJ, 225, 357

Semboloni, E., Schrabback, T., van Waerbeke, L., et al. 2011, MNRAS, 410, 143

Skibba, R. A., van den Bosch, F. C., Yang, X., et al. 2011, MNRAS, 410, 417

Sofue, Y., & Rubin, V. 2001, ARA&A, 39, 137

Spergel, D. N., Bean, R., Doré, O., et al. 2007, ApJS, 170, 377

Springel, V., White, S. D. M., Jenkins, A., et al. 2005, Nature, 435, 629

Umetsu, K., Medezinski, E., Nonino, M., et al. 2014, arXiv:1404.1375

van Albada, T. S., Bahcall, J. N., Begeman, K., & Sancisi, R. 1985, ApJ, 295, 305

van den Bosch, F. C., Norberg, P., Mo, H. J., & Yang, X. 2004, MNRAS, 352, 1302

van den Bosch, F. C., Weinmann, S. M., Yang, X., et al. 2005, MNRAS, 361, 1203

van Uitert, E., Hoekstra, H., Schrabback, T., et al. 2012, A&A, 545, A71

von der Linden, A., Best, P. N., Kauffmann, G., & White, S. D. M. 2007, MNRAS, 379, 867

Wilman, D. J., Balogh, M. L., Bower, R. G., et al. 2005, MNRAS, 358, 71

Wright, C. O., & Brainerd, T. G. 2000, ApJ, 534, 34

Yang, X., Mo, H. J., van den Bosch, F. C., & Jing, Y. P. 2005a, MNRAS, 356, 1293

Yang, X., Mo, H. J., van den Bosch, F. C., et al. 2005b, MNRAS, 362, 711

Yang, X., Mo, H. J., van den Bosch, F. C., et al. 2007, ApJ, 671, 153

Zabludoff, A. I., & Mulchaey, J. S. 1998, ApJ, 496, 39

Zaritsky, D., Smith, R., Frenk, C., & White, S. D. M. 1993, ApJ, 405, 464

Zaritsky, D., & White, S. D. M. 1994, ApJ, 435, 599

Zaritsky, D., Smith, R., Frenk, C., & White, S. D. M. 1997, ApJ, 478, 39

Zwicky, F. 1937, ApJ, 86, 217

Chapter 2

Methodology

In this chapter the basics of gravitational lensing are presented followed by a detailed description of the two analysis methods used in this work: the weak lensing method (see Section 2.2) and the dynamical method (see Section 2.3).

2.1 Gravitational Lensing

Gravitational lensing is a fundamental prediction of general relativity. Clustered mass acts like a lens and induces a distortion of local space-time which causes the gravitational lensing phenomena. Consequently the shape of background objects (referred to as sources) that reside behind a massive foreground system (referred to as lenses) appear elongated tangentially with respect to the centre of the perturber (see Figure 2.1). Gravitational lensing is divided into two regimes: *strong gravitational lensing* (see Figure 2.1b) and *weak gravitational lensing* (see Figure 2.1c). Each reveals different information about the foreground system. Further details on gravitational lensing can be found in the extensive reviews of Schneider et al. (1992) and Blandford & Narayan (1992).

Strong gravitational lensing may result in magnification of the galaxy source and distortion of its shape (see Figure 2.2a). It also causes multiple images of extended or point sources (see Figure 2.2b).

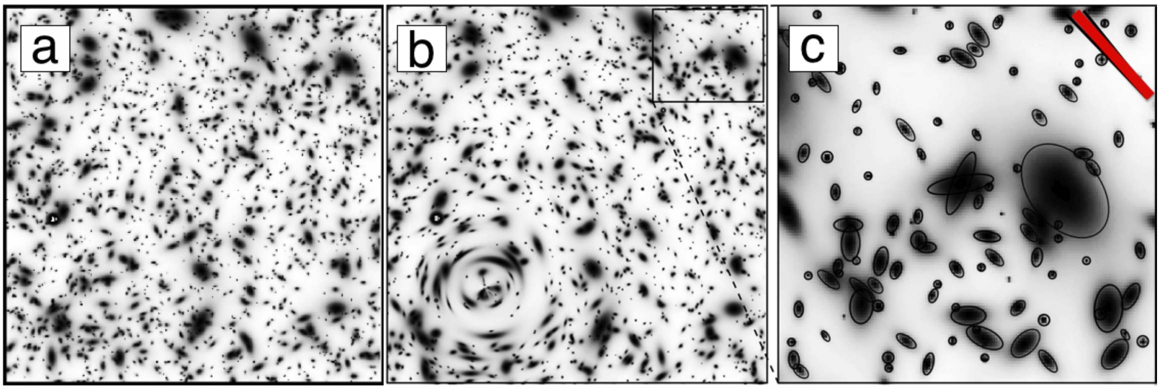

Figure 2.1: From Mellier (1999) and Fort & Mellier (1994) a) a field without gravitational lensing, b) a field sky with simulated presence of massive system causing strong gravitational lensing in the lower left corner of the panel, c) zoom-in on a weak lensing regime from the middle panel where the average alignment of the galaxy shape (red line) is tangential to the location of the lens.

Strong lensing allows the measurement of mass in a lens at small radii which can be extracted from Einstein radius (θ_E) where the distances of lens and the source are known. From the Schwarzschild metric one can find the following relation for the angle of deflection:

$$\alpha = \frac{4G}{c^2}\frac{M}{\xi} \tag{2.1}$$

where c is the speed of light, G is the universal gravitational constant, M is the mass of the lens, and ξ is the impact parameter (see Figure 2.3). If the impact parameter is large then the magnification and distortion are weaker. It is possible to rearrange Equation 2.1, noting that, if $\xi << D_L$, then $\sin(\theta) \sim \theta = \xi/D_L$, where D_L is the distance between us and the lens, D_S is the distance between us and the source, D_{LS} is the distance between the lens and the source. By considering the equality $\theta D_s = \beta D_S + \alpha D_{LS}$, we can compare this equation to Equation 2.1 by isolating α. The maximum distortion is reached when the objects are perfectly aligned which means $\beta = 0$ and $\theta = \theta_E$. We then get a complete circle. The radius of this circle θ_E is given by:

$$\theta_E = \left(\frac{4GM}{c^2}\frac{D_{LS}}{D_S D_L}\right)^{1/2} \tag{2.2}$$

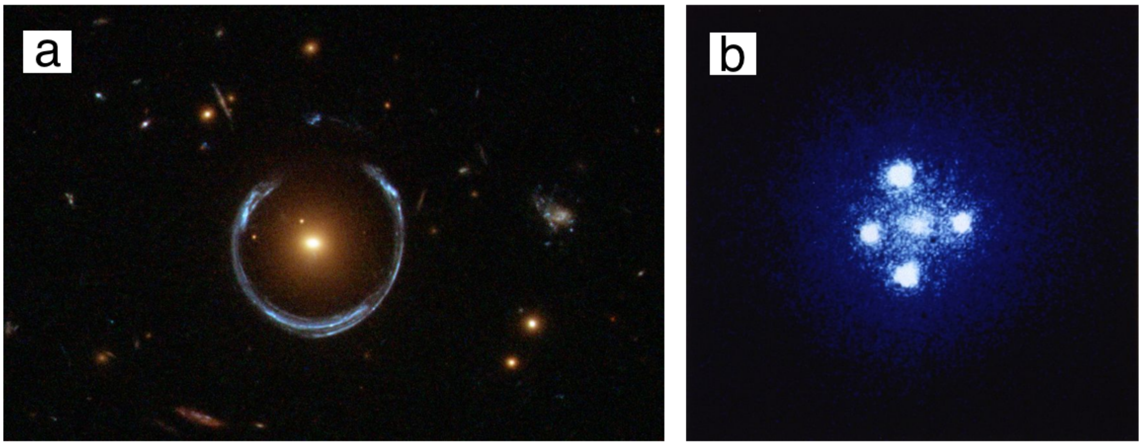

Figure 2.2: a) Horseshoe LRG 3-757 is an example of the distortion caused by strong gravitational lensing which results in an Einstein ring b) Einstein cross QSO 2237+0305 is a famous example of multiply imaged quasar, Images Credit: ESA/Hubble & NASA (left figure), NASA,ESA & STScl (right figure).

As can be seen in Equation 2.2, the distortion of background galaxies depends on the distance to the lens and the source and the mass of the lens.

The first identified gravitationally lensed object was observed in 1979 with the discovery of the candidates QSO 0957+561A and B. The two sources were both images of the same quasar gravitationally lensed by the presence of a giant elliptical galaxy (Walsh et al., 1979). Later, other lensing detections were confirmed (e.g. Lynds & Petrosian, 1989; Soucail et al., 1988) with the discovery of several arcs (see Figure 2.1a) in compact clusters.

Strong lensing is commonly used to trace the inner part of DM halos. Precise cluster mass estimates on small scales have been provided using multiple images and arcs (Hammer, 1991; Kneib et al., 1996). However, arcs mostly occur around high central mass concentrations; moreover, strong lensing is mostly detected around very massive clusters or giant elliptical galaxies.

2.2 Weak Lensing Methodology

Background sources with large impact parameters or sources behind low mass lenses are typically not strongly lensed and instead are in the weak lensing regime (see Figure 2.1c).

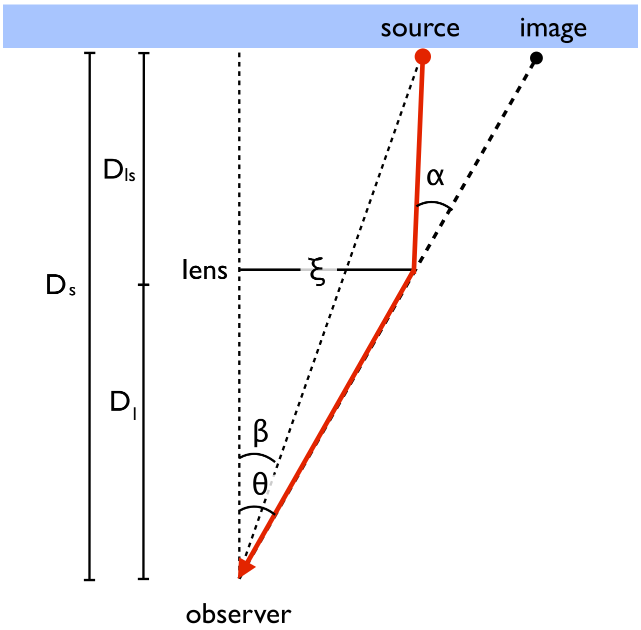

Figure 2.3: Diagram of the gravitational lensing configuration where θ is the angular position of the background galaxy as seen by the observer and β is the real angular position

Weak gravitational lensing is detected through the measurement of the distortion in the shape of background galaxies. The strength of the distortion can be measured as a function of the distance from a given centre hence DM halo properties can be extracted using an appropriate dark matter density model.

It is possible to measure the statistical distortion in image ellipticity through high quality imaging. As the distortion depends strongly on the mass of the system, the signal of individual low mass systems is too small to be detected. Even with the much higher source density from HST observations, it is not possible to extract the weak lensing signal around an individual galaxy or low mass group. By stacking the signal from a large ensemble of lenses (see Fig 2.4), it is possible to improve the signal-to-noise (S/N) of the measurement. Early studies of weak lensing were based on small surveys (Brainerd et al., 1996; Hudson et al., 1998). Large survey areas such as the SDSS remarkably improved the signal detection by increasing the number of lens-source pairs (e.g. Fischer et al., 2000). Deep observations also provide the possibility of improving the accuracy of the lensing signal by detecting more distant galaxies hence increasing the number of sources (Hoekstra et al., 2004; Parker et al., 2007). Since the first detection of a weak lensing signal (Brainerd et al., 1996), this technique has been used by many authors for statistical analysis around galaxies (e.g Fischer et al., 2001; Smith et al., 2001; Hoekstra et al., 2004; Parker et al., 2007) and around clusters (e.g. Johnston et al., 2007; Sheldon et al., 2009). However, there are relatively few weak lensing analyses around galaxy groups (e.g. Hoekstra et al., 2001; Parker et al., 2005).

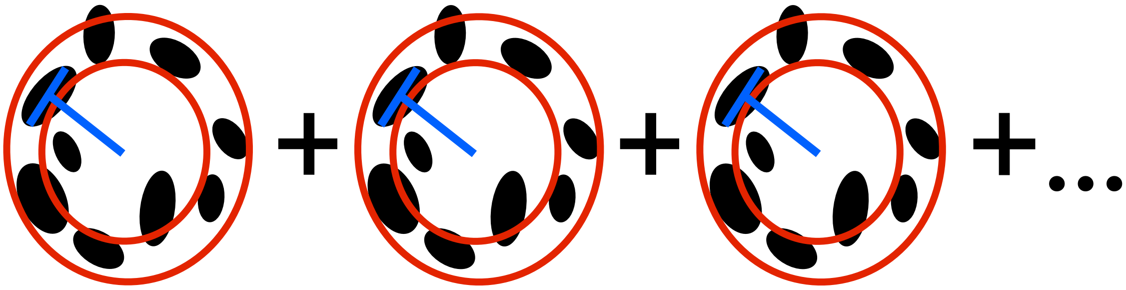

Figure 2.4: Diagram of the stacked signal of many galaxy groups where the black ellipses represent the background galaxies and red circles represent the annular bins. The measurement of the tangential component of the background galaxy relative to the centres is illustrated in blue.

Today, weak lensing is a powerful method which provides information on the properties (e.g. mass, shape, density profile) of dark matter halos and is also used as a tool to probe the inhomogeneity of the mass distribution of the Universe at large scales (Massey et al., 2007; Fu et al., 2008; Schrabback et al., 2010). This technique is convenient to probe dark matter halos' density profiles at large radii while strong lensing is best to evaluate the mass contained within a small region of a system. The main advantage of weak galaxy-galaxy lensing compared to dynamical methods is that it is independent of assumptions about the dynamical state of the system.

The main drawbacks of the weak lensing method are: the weakness of the signal, the deterioration of the signal caused by unrelated projected mass along the line-of-sight between the lens and the observer, the sensitivity to the choice of centering, and the requirement of reasonable assumptions to convert 2-D projected mass distribution into a 3-D mass distribution.

2.2.1 Galaxy Shape Measurements

Galaxy shapes on the sky can be described by their ellipticity and orientation, which in turn can be parameterized by two-components: e_1 and e_2, following the Blandford et al. (1991) terminology (see Figure 2.5). Those two parameters are defined by the weighted quadrupole moments method as in the KSB method (Kaiser et al., 1995):

$$e_1 = \frac{I_{11} - I_{22}}{I_{11} + I_{22}}, e_2 = \frac{2I_{12}}{I_{11} + I_{22}} \tag{2.3}$$

where I_{ij} are the quadrupole moments which are found using the surface brightness of the galaxies. The location of the sources' centres are determined by their peak in luminosity once the images are smoothed.

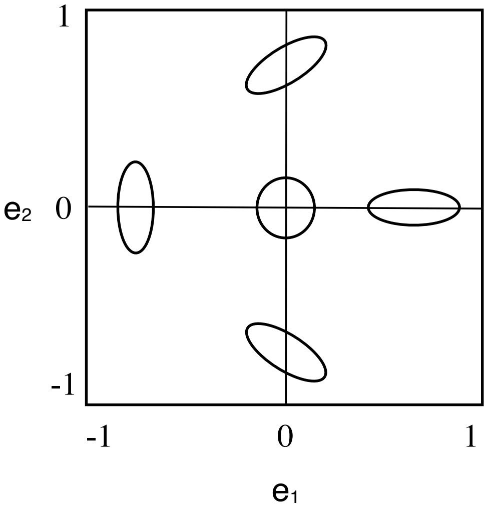

Figure 2.5: Adapted from Kaiser et al.(1995), polarization and orientations of galaxies as a function of their polarization parameters e_1 and e_2

From Equations 2.3, the ellipticity of each galaxy is given by:

$$e = \sqrt{e_1^2 + e_2^2} \tag{2.4}$$

Theoretically, the ellipticity should be between 0 and 1, where 0 corresponds to a circular galaxy and 1 corresponds to a very elongated galaxy. We expect the mean ellipticity of the shape measurement for a large sample of galaxies in a random field to be zero. On the other hand, with the presence of a lens galaxy, we expect the mean shape of the background galaxies in the surrounding area to be elliptical with a tangential orientation relative to the lens (see Figure 2.1c). The orientation of the background galaxy ϕ_s (see Figure 2.6) can be found from:

$$\phi_s = \frac{1}{2}\arctan\left(\frac{e_1}{e_2}\right) \tag{2.5}$$

The factor of 1/2 stems from the definition of the ellipticity where $\theta = 180°$ is associated with a rotation of 90° (see Figure 2.5).

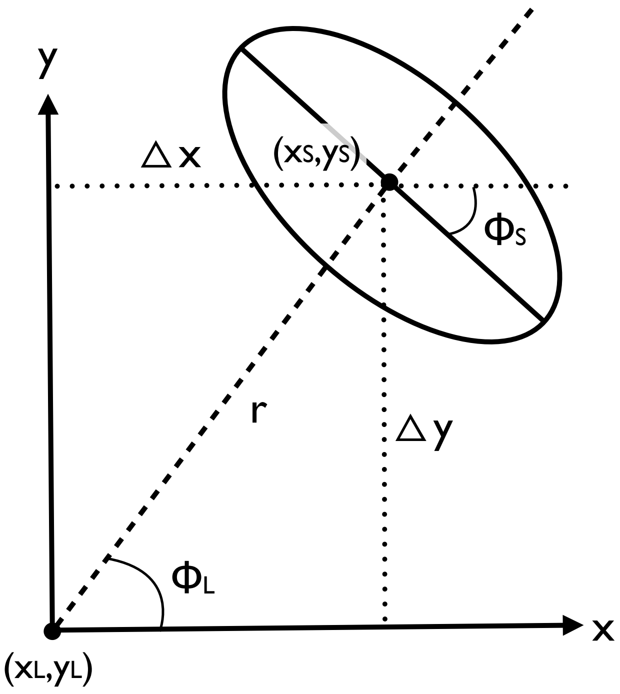

Figure 2.6: Orientation of the background galaxy relative to the centre of the lens where the tangential component of the background galaxy shape is represented in dashed line. (x_S, y_S) and (x_L, y_L) are the co-ordinate of the source and the centre of the foreground lens respectively.

The position of the background galaxy and the location of the centre of the lens are required as one needs the orientation of the vector connecting the lens and the source to evaluate the tangential component of the source. The orientation of the background galaxy relative to the centre of the lens (see Figure 2.6) is defined as:

$$\phi_L = \arctan\left(\frac{\Delta y}{\Delta x}\right) \tag{2.6}$$

where the position of the centre of the lens is (x_L, y_L) and the position of the centre of the source is (x_S, y_S). Therefore, the vector $\vec{r} = (\Delta x, \Delta y)$ is defined as $\vec{r} = (-(x_S - x_L)\cos(y_L)\ \hat{x}, (y_S - y_L)\ \hat{y})$. In order to take into account the projection of the sky, a minus sign needs to be added to the RA. The cosine factor must be introduced to account for the non-euclidean shape of the sky.

Finally, the tangential component of the background galaxy relative to a given centre, also referred to as the *shear*, is given by:

$$e_T = -\frac{e}{P_\gamma}\cos(2(\phi_s - \phi_L)) \tag{2.7}$$

where multiple improvements of the polarization measurements have been achieved in Hoekstra et al. (1998) by introducing the shear polarizability parameter P_γ. This parameter takes into account the degradation of faint galaxy images caused by the effect of seeing, camera distortion, and point spread function (PSF) anisotropy which smears the images. As these effects are blurring the shape of the background galaxy, the true ellipticity of the galaxies is underestimated. The factor P_γ is introduced in order to compensate for the degradation of the images and is defined as in Fischer et al. (2000).

2.2.2 Shear Measurement

We are interested in the variation of the tangential ellipticity e_T as a function of the distance from the centre of mass. This relation enables us to extract dark matter halo properties. The mean tangential shear is weighted by the error in the shape measurement as follows:

$$\langle\gamma_T\rangle = \frac{\sum_i e_{T,i} w_i}{\sum_i w_i} \tag{2.8}$$

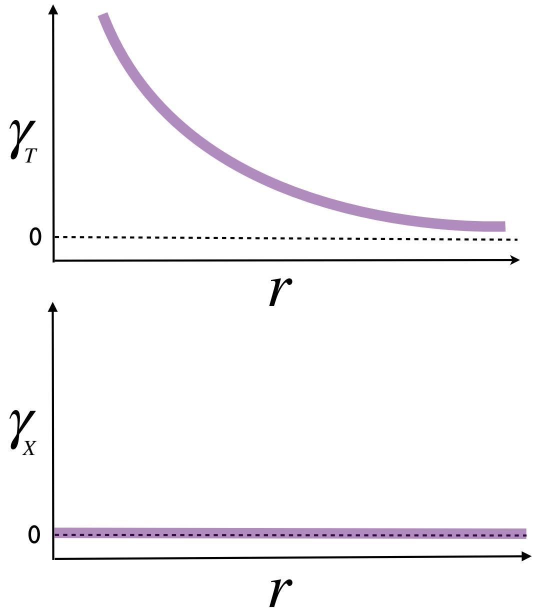

Figure 2.7: Schematic illustration of an ideal shear profile as a function of the distance from the foreground lens centre (top panel) and cross-shear (bottom panel).

where $e_{T,i}$ is the tangential component of the galaxy i and w_i is its error measurement in the shape $\left(w_i = \frac{1}{\sigma_{e,i}^2+\sigma_{SN}^2}\right)$, where $\sigma_{SN} = 0.32$ is the shape noise for the galaxies[1] and $\sigma_{e,i}$ is the uncertainty on the shape of the galaxies. By stacking all groups around their given centres, one can evaluate the mean tangential shear within annuli.

After calculating the mean shear in annular bins, it is possible to extract a radial profile for the tangential shear. In the top panel of Figure 2.7, we illustrate a schematic of tangential shear $\langle\gamma_T\rangle$ as a function of the projected distance from the foreground lens centre. The signal is expected to decrease as a function of the distance from the lens. In order to verify that the tangential signal detected is really due to gravity, one can rotate the source images by 90° and expect the so-called cross-shear (γ_X) to vanish. The schematic of the cross-shear is illustrated in the bottom panel of Figure 2.7.

The approach used to test different candidate centres using weak lensing is illustrated in Figure 2.8. Two candidates centres are compared (blue and purple). The blue candidate is

---

[1] The shape noise is an estimate of the ensemble averaged ellipticity of the entire galaxy sample.

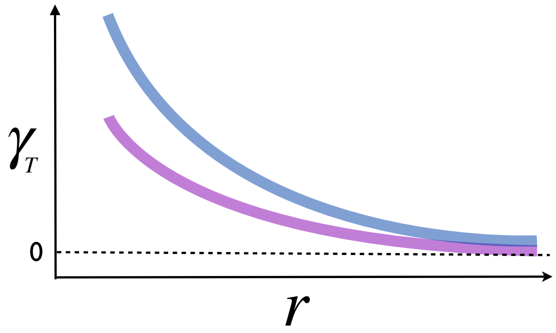

Figure 2.8: Schematic illustration of lensing around two difference candidate centres where the blue centre definition is better than the purple one.

closer to the real centre definition than the purple one. This difference affects the amplitude of the signal as the signal around the blue centre definition reaches higher shear values on small scales. Consequently, one would say that the blue centre definition is better at tracing the centre of mass than the purple one. Our aim is to find which centre definition maximizes the lensing signal at small scales.

2.2.3 Models

In order to obtain physical properties of dark matter halos, the tangential shear profile needs to be fitted by an assumed halo mass model. The tangential shear can be related to the contrast in mass density (Wright & Brainerd, 2000):

$$\gamma_T(R) = \frac{\overline{\Sigma}(< R) - \Sigma(R)}{\Sigma_c} \tag{2.9}$$

where R is the projected radius relative to the centre, $\Sigma(R)$ is the projected surface mass density at position R from the centre, $\overline{\Sigma}(< R)$ is the mean projected surface mass density within the radius R and Σ_c is the critical surface mass density and is given as:

$$\Sigma_c = \frac{c^2}{4\pi G}\frac{D_S}{D_L D_{LS}} \tag{2.10}$$

where c is the speed of light, G is the universal gravitational constant, and D_S, D_L and D_{LS} still correspond to the angular diameter distance of the source, the lens and between the lens and the source, respectively.

The surface mass density is obtained by integrating the volume mass density profile along the line-of-sight with the assumption that the density profile is spherically symmetric:

$$\Sigma(R) = 2\int_0^\infty \rho(R,z)dz \tag{2.11}$$

as ρ is an even function, we fix the boundaries to positive values by adding a factor of 2 to the integral. By introducing a density profile into the projected surface mass density, one can obtain a shear model. The simplest model is the SIS (see Equation 1.1) introduced in Section 1.1.2. Assuming that the DM halo is a SIS density profile, the tangential shear is given by:

$$\gamma_{SIS}(\theta) = \frac{2\pi\sigma^2\beta}{c^2\theta} = \frac{\theta_E}{2\theta} \tag{2.12}$$

where σ is the intrinsic velocity dispersion, c is the speed of light, θ is the angular distance and can be expressed in physical units using the relation $\theta = R/D_L$ where R is the projected distance, and θ_E is the Einstein radius which can be simplified to:

$$\theta_E = \frac{4\pi\sigma^2\beta}{c^2} = \left(\frac{\sigma}{186\mathrm{km/s}}\right)^2 \beta[\mathrm{arcsec}] \tag{2.13}$$

where $\beta = D_{LS}/D_S$ is the ratio of the angular diameter distances. From this model one can extract σ and therefore estimate the mass from Equation 1.2 if the systems sizes are known.

A more complex and universal model is the NFW profile (see Equation 1.3). The tangential shear using NFW density profile was calculated in Wright & Brainerd (2000). The shear for the NFW profile depends on two free parameters: the virial size R_{200} and the concentration parameter c. In order to get a one-parameter fit, it is possible to fix the value of the concentration c.

2.3 Dynamical Methodology

Dynamics can be used to find the mass of a system of particles. This technique probes the depth of the gravitational potential well using the motions of visible tracers. In galaxy groups and clusters, it is possible to use the radial velocities of member galaxies to estimate the halo mass if one makes reasonable assumptions about the dynamical state of the system and the orbits of the member galaxies. This method, just as the weak lensing method, is sensitive to the choice of centering. Hence, the dynamical method represents an alternative technique to probe centering in groups and provides us the opportunity to compare the results from both techniques.

Assuming a stable system of particles such as stars or galaxies, the velocity dispersion of this system can be approximately related to its total mass as follows from the virial theorem:

$$\sigma^2 \propto \frac{M}{R} \tag{2.14}$$

where σ, M and R are the velocity dispersion, mass and size of the system, respectively. One way to probe the mass distribution of galaxy groups is to examine the velocity of the members galaxies as a function of the radius with respect to the centre.

The main drawbacks of this technique are: the lack of visible tracers (as groups typically have few members), the assumption of dynamical equilibrium, and the requirement of a reasonable assumption to convert the projected velocity dispersion profile into a mass profile. In a similar approach to the weak lensing analysis, in order to counter the low S/N or poor statistics, one can stack many systems together in order to accumulate sufficient statistics to study the velocity dispersion profiles. This technique has been used to show that there are extend DM halos around galaxies by looking at the radio velocities of satellite galaxies (Zaritsky et al., 1993; Zaritsky & White, 1994; Zaritsky et al., 1997; McKay et al., 2002; Prada et al., 2003).

2.3.1 Velocity Dispersion Profile (VDP)

In order to evaluate which centre definition best traces the location of the centre of the potential well, one can evaluate the velocity dispersion profile (hereafter VDP), which consists of the projected velocity dispersion profile as a function of group-centric radius. By stacking many systems using a given centre definition, this technique enables us to trace the averaged mass distribution in groups. As observations are restricted to only one component of the velocity of the members galaxies, i.e. the radial velocity extracted from the redshift, we assume that the systems are spherical and isotropic. Therefore, the velocity of the member is defined as $v_{\rm mem} = c \times \Delta z = c \times (z_{\rm centre} - z_{\rm mem})$. Assuming systems in dynamical equilibrium, the VDP is expected to monotonically decrease as the distance from the centre increases as shown is Figure 2.9 where the system is divided in three annuli (blue, green and orange). At small distance from the centre (blue annuli), the velocity of the member span a large range. Therefore the velocity dispersion is high. At large distance (orange annuli), the velocity of the member is close to zero hence, the VDP is expected to decrease as a function of the radius from the centre. However, we mentioned previously (see Section 1.3) that young groups or groups in process of accreting can be far from dynamical equilibrium. This issue is discussed in Section 3.4.2.

Bergond et al. (2006) proposed a method of measuring the velocity dispersion profile which involves exponentially weighting the member as a function of their distance from a bin (see Equation 2.15 and 2.16). In comparison to the traditional binning techniques which lead to noisy profiles, this *moving window* prescription generates a smoothed profile. The Bergond et al. method is convenient for small samples as it takes into account the contribution of every member in each individual point. The method outlined in Bergond et al. starts with defining the velocity dispersion profile with radius as:

$$\sigma(R) = \sqrt{\frac{\sum_i w_i(R)(x_i - \bar{x})^2}{\sum_i w_i(R)}} \tag{2.15}$$

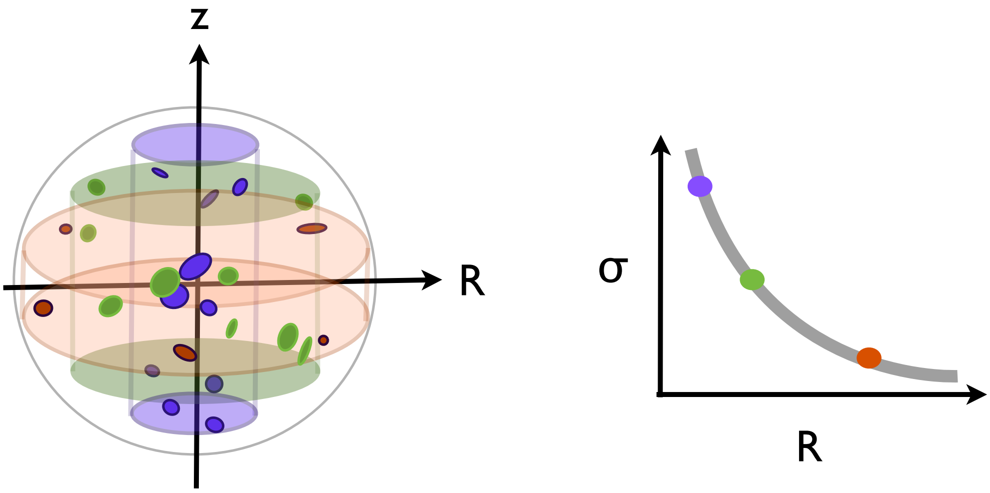

Figure 2.9: Schematic illustration of the VDP where the system is divided in three annular bins (blue, green and orange) in the left panel. The galaxies in the blue bins span the larger range in redshift and the galaxies in the orange bins span the smaller range in redshift. As we assume the velocity of the member to be proportional to Δz the velocity dispersion (σ) is expected to decrease as a function of the distance. The velocity dispersion for the blue, green and orange bin is illustrate in the right panel.

where x_i's is the radial velocity of the members and $\bar{x}$ is the mean velocity the system. The weight $w_i(R)$ is defined as:

$$w_i(R) = \frac{1}{\sigma_R}\exp\left[\frac{-(R-R_i)^2}{2\sigma_R^2}\right] \tag{2.16}$$

where R is the radial position from the centre, the R_i's are the radial position of the members of the system and σ_R is the width of the window.

The approach used to test which centre best traces the centre of the potential is illustrated in in Figure 2.10 where the schematic VDPs of two different centre definitions are compared. The legend is the same as in Figure 2.8 (blue definition is closer to the real centre). The signal around the blue candidate is rising up on small scales while a turn over is observed around the purple candidate centre. This turn over is related to the offset between the real centre and the candidate centre.

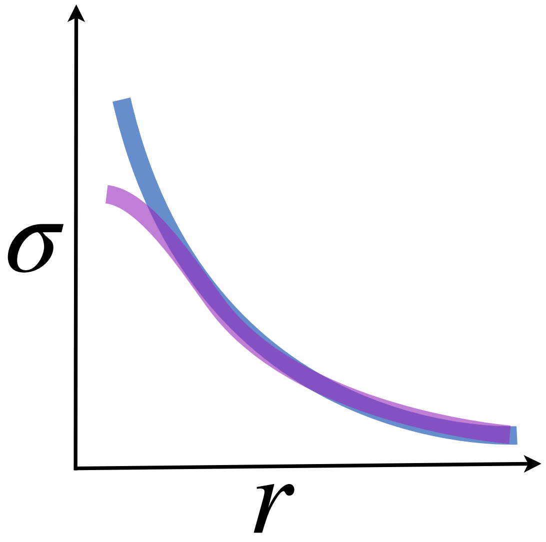

Figure 2.10: Schematic illustration of the VDP around two different centre candidates where the blue candidate centre is closer to the real centre than the purple.

Bibliography

Bergond, G., Zepf, S. E., Romanowsky, A. J., Sharples, R. M., & Rhode, K. L. 2006, A&A, 448, 155

Blandford, R. D., Saust, A. B., Brainerd, T. G., & Villumsen, J. V. 1991, MNRAS, 251, 600

Blandford, R. D., & Narayan, R. 1992, ARA&A, 30, 311

Brainerd, T. G., Blandford, R. D., & Smail, I. 1996, ApJ, 466, 623

Bullock, J. S., Kolatt, T. S., Sigad, Y., et al. 2001, MNRAS, 321, 559

Fischer, P., McKay, T. A., Sheldon, E., et al. 2000, AJ, 120, 1198

Fischer, P., McKay, T. A., Sheldon, E., & SDSS Collaboration 2001, Gravitational Lensing: Recent Progress and Future Go, 237, 395

Fort, B., & Mellier, Y. 1994, A&A Rev., 5, 239

Fu, L., Semboloni, E., Hoekstra, H., et al. 2008, A&A, 479, 9

Hammer, F. 1991, ApJ, 383, 66

Hoekstra, H., Franx, M., Kuijken, K., & Squires, G. 1998, ApJ, 504, 636

Hoekstra, H., Franx, M., Kuijken, K., et al. 2001, ApJ, 548, L5

Hoekstra, H., Yee, H. K. C., & Gladders, M. D. 2004, ApJ, 606, 67

Hudson, M. J., Gwyn, S. D. J., Dahle, H., & Kaiser, N. 1998, ApJ, 503, 531

Johnston, D. E., Sheldon, E. S., Wechsler, R. H., et al. 2007, arXiv:0709.1159

Kaiser, N., Squires, G., & Broadhurst, T. 1995, ApJ, 449, 460

Kneib, J.-P., Ellis, R. S., Smail, I., Couch, W. J., & Sharples, R. M. 1996, ApJ, 471, 643

Lynds, R., & Petrosian, V. 1989, ApJ, 336, 1

Massey, R., Rhodes, J., Leauthaud, A., et al. 2007, ApJS, 172, 239

McKay, T. A., Sheldon, E. S., Johnston, D., et al. 2002, ApJ, 571, L85

Mellier, Y. 1999, ARA&A, 37, 127

Parker, L. C., Hudson, M. J., Carlberg, R. G., & Hoekstra, H. 2005, ApJ, 634, 806

Parker, L. C., Hoekstra, H., Hudson, M. J., van Waerbeke, L., & Mellier, Y. 2007, ApJ, 669, 21

Prada, F., Vitvitska, M., Klypin, A., et al. 2003, ApJ, 598, 260

Schneider, P., Ehlers, J., & Falco, E. E. 1992, Gravitational Lenses, XIV, 560 pp. 112 figs.. Springer-Verlag Berlin Heidelberg New York. Also Astronomy and Astrophysics Library,

Schrabback, T., Hartlap, J., Joachimi, B., et al. 2010, A&A, 516, A63

Sheldon, E. S., Johnston, D. E., Masjedi, M., et al. 2009, ApJ, 703, 2232

Smith, D. R., Bernstein, G. M., Fischer, P., & Jarvis, M. 2001, ApJ, 551, 643

Soucail, G., Mellier, Y., Fort, B., Mathez, G., & Cailloux, M. 1988, A&A, 191, L19

Walsh, D., Carswell, R. F., & Weymann, R. J. 1979, Nature, 279, 381

Wright, C. O., & Brainerd, T. G. 2000, ApJ, 534, 34

Zaritsky, D., Smith, R., Frenk, C., & White, S. D. M. 1993, ApJ, 405, 464

Zaritsky, D., & White, S. D. M. 1994, ApJ, 435, 599

Zaritsky, D., Smith, R., Frenk, C., & White, S. D. M. 1997, ApJ, 478, 39

Chapter 3

Data

In this chapter, we describe the GEEC group catalog (see Section 3.2) which is based on the CNOC2 catalog (see Section 3.1). In Section 3.3, we define the candidate group centres and in Section 3.4, we present the selected group samples. We discuss the offset between the centre candidates in Section 3.4.1 and in Section 3.4.2 we described the implications of dynamical complexity in groups. In order to achieve our goal of studying the location of group centres with weak lensing, images of reasonable quality and depth are required while dynamical analysis needs high spectroscopic completeness. The galaxy shape measurements have been done by Parker et al. (2005) and Finoguenov et al. (2009) where the background galaxy images were obtained from CFHT and the 4m KPNO/Mayall telescope images (Parker et al., 2005). The numerous GEEC spectroscopic campaigns used in the VDP analysis are described in detail in Section 3.2.1.

3.1 The CNOC2 survey

The primary goal of the original CNOC2 survey consisted of studying galaxy populations, clustering and evolution for non-cluster fields. This spectroscopic and photometric survey consists of five image bands U, B, V, R_C, I_C (Yee et al., 2000). The CNOC2 survey is composed of four fields widely separated on the sky: $RA02h$, $RA09h$, $RA14h$ and $RA21h$ where the names refer to their right ascension position. This distribution is designed to avoid cosmic variance issues and guarantee year-round observations. The four patches covered a total area of ∼1.5 deg^2 of the sky with ∼0.4 deg^2 per patch, and approximately 10^4 galaxies confined in a volume of $10^6 h^{-3}\mathrm{Mpc}^3$ were observed. Over 6000 spectroscopic redshifts were obtained down to a limiting magnitude of $R_c = 21.5$ and with 48% completeness (Yee et al., 2000). The spectroscopic survey was conducted with the Multi-Object Spectrograph (Le Fevre et al., 1994, MOS,) at the 3.6m Canada-France-Hawaii Telescope (CFHT). Each MOS field covers about 70 arcmin^2 (0.02 deg^2) hence about 20 MOS fields were needed per patch. The geometric shape of the patches (see Figure 3.1) were designed to accurately determine the correlation function.

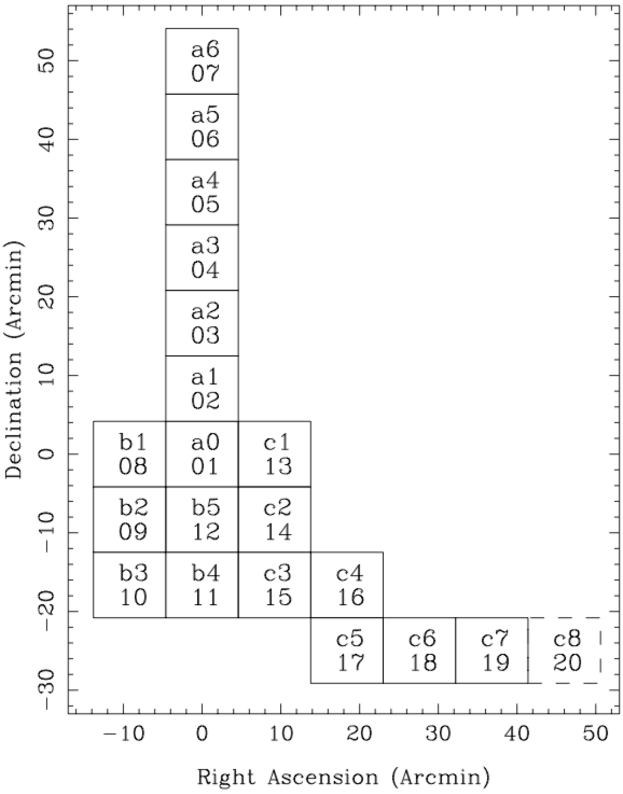

Figure 3.1: From Yee et al.(2000) Designed of the CNOC2 patches

Galaxy groups from the CNOC2 survey were identified using the Friends-of-Friends (hereafter F-O-F) method developed by Huchra & Geller (1982), which locates over densities in projection and in redshift space (Carlberg et al., 2001). This technique can be tuned to find very different systems from compact and fully virialized to loose group populations. The F-O-F algorithm starts with any galaxy as the beginning of a trial group and looks for galaxies within a given projected ($\mathrm{R}_{\mathrm{max}}$) and velocity separation ($\mathrm{V}_{\mathrm{max}}$). If galaxies are found then a new group i is created and the search for new companion continue. This procedure continues until there are no more galaxies added to the groups or until a stable velocity dispersion is reached. Figure 3.2 represents the basic step of the algorithm. Roughly 200 groups were identified from the CNOC2 survey in redshift range $0.12 < z < 0.55$ (Carlberg et al., 2001).

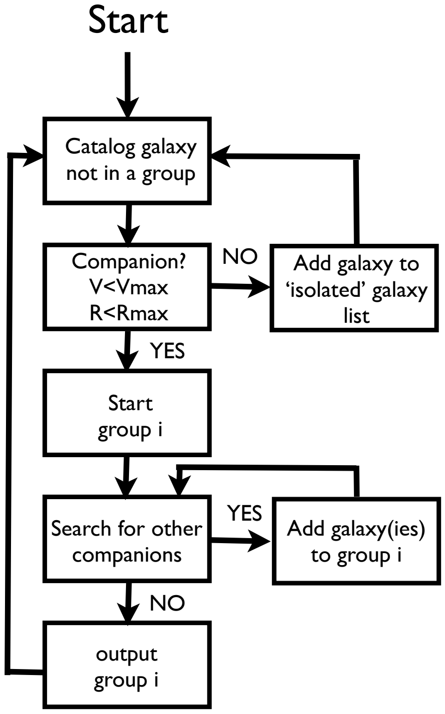

Figure 3.2: Adapted from Huchra & Geller (1982) schematic of F-O-F algorithm

The velocity dispersions of the CNOC2 groups were calculated in Wilman et al. (2005) and later recomputed in Connelly et al. (2012) for the GEEC catalogs[1]. For small number statistics, the standard deviation tends to overestimate the velocity dispersion. Hence, Beers et al. (1990) recommend the Gapper Estimator in order to evaluate the velocity dispersion, which is less sensitive to the outliner data points than the standard deviation. The Gapper algorithm is given by:

$$\sigma(z)_{Gapper} = 1.135c\Big(\frac{\sqrt{\pi}}{n(n-1)}\sum_{i=1}^{n-1} w_i g_i\Big) \tag{3.1}$$

where $w_i = i(n-i)$ and $g_i = \times(z_{1+i} - z_i)$. The z$_i$ values are the sequentially ordered redshifts of the galaxy members and c is the speed of light. As only the members within 2σ of the Gaussian

---

[1] The velocities dispersion of the GEEC groups can be found in Tables 4-6 in Connelly et al. (2012).

velocity distribution[2] are considered, this clipping gives an underestimated value of the true velocity dispersion. The multiplicative factor 1.135 is required to account for the 2σ clipping of a Gaussian velocity distribution.

3.2 The GEEC catalog

In order to improve the group data set, extensive follow-up spectroscopic surveys (Wilman et al., 2005; Balogh et al., 2011; Connelly et al., 2012) and multi wavelength observations in the near-infrared (Balogh et al., 2007; Wilman et al., 2008; Balogh et al., 2009), optical (Balogh et al., 2009), ultraviolet (McGee et al., 2011) and X-ray (Finoguenov et al., 2009) were executed. These multiple complementary campaigns have been combined into a new data set called the GEEC group catalog.

3.2.1 Extensive Follow-up Observations

Extensive follow-up spectroscopy was executed on the 6.5m Magellan telescope at Las Campanas Observatory (LCO) in Chile (Wilman et al., 2005) with the aim of improving the membership completeness and depth of the initial CNOC2 group catalog. This large telescope is equipped with a better spectrograph, and gives the opportunity to measure redshifts of faint galaxies that were originally undetectable in the CNOC2 survey. Three of the four patches were covered by 20 *Low Dispersion Survey Spectrograph* (LDSS-2) fields. In total 392 additional redshifts were obtained, improving the redshift completeness to 74% and raising the limiting magnitude to $R_c = 22$. After inclusion of these additional redshifts, membership was reassigned (Wilman et al., 2005). The original F-O-F parameters were tuned to find virialized cores. The new criteria defined in Wilman et al. allowed the identification of more loosely bound groups by adding galaxies with a higher projected distance to the group. Therefore, compact groups are not affected by this change, while other groups gained extra members.

---

[2] For more detail about the Gaussian velocity distribution see Section 3.4.2.

Near-infrared observations were executed with the *Isaac Newton Group Red Imaging Device* (INGRID) on the William Herschel Telescope (WHT) (Balogh et al., 2007) along with the *Infrared Array Camera* (IRAC) on Spitzer (Balogh et al., 2007; Wilman et al., 2008). The near-infrared band, which is very weakly star formation dependent, is commonly used to trace the stellar mass. The first estimations of the stellar mass of the group member have been investigated in Balogh et al.(2007), where they was computed using Bruzual & Charlot (2003) models and assuming a Chabrier (2003) initial mass function. Additional optical imaging from HST-ACS was also used to evaluate the morphology of the galaxy members (Wilman et al., 2009). Complementary optical imaging from two wide-field mosaic cameras CFH12k and Megacam were obtained on the CFHT and new near-infrared data were taken with the NTT-SOFI (Balogh et al., 2009).

In order to detect the presence of hot gas in groups, and to find groups outside the original CNOC2 redshift range, deep X-ray images of two of the GEEC fields (14h and 21h) were obtained with the $XMM-Newton$ and *Chandra* space telescopes (Finoguenov et al., 2009). XMM is ideal for finding faint extended sources while Chandra can locate point sources, such as active galaxy nuclei (AGN). Groups were detected out to a redshift of ∼0.85. These extra X-ray luminous group detections along with the previous spectroscopically selected groups from the CNOC2 were now combined into the new large GEEC group catalog. This combination allows the access to a group catalog with a full range of dynamical states with a large redshift range. The previous detailed optical and near-infrared photometric observations did not cover much of area observed in the X-ray. Hence, supplementary infrared observations with the WIRCAM on CFHT were obtained and the stellar masses were recomputed from SED-fitting (McGee et al., 2011). Furthermore, because spectroscopic memberships for newly identified X-ray groups were not available, additional spectra were obtained with the IMACS on the 6.5m-Baade Magellan Telescope and with the FORS2 on the VLT (Connelly et al., 2012) with an additional contribution from GMOS on the Gemini telescope (Balogh et al., 2011). This last observation was targeting only one group as part of an ongoing study of galaxy groups at high redshift. These three extra contributions added 1946 previously unknown secure redshifts.

3.3 Definition of candidate centres

Studying the distribution of dark matter in galaxy groups is possible with the use of techniques such as strong lensing, weak lensing and dynamics. However these techniques critically depend on the assumption of the halo centre's location. The aim of this project is to analyze the sensitivity to the choice of centering by using different centre definitions and determine which one most accurately traces the centre of DM mass distribution.

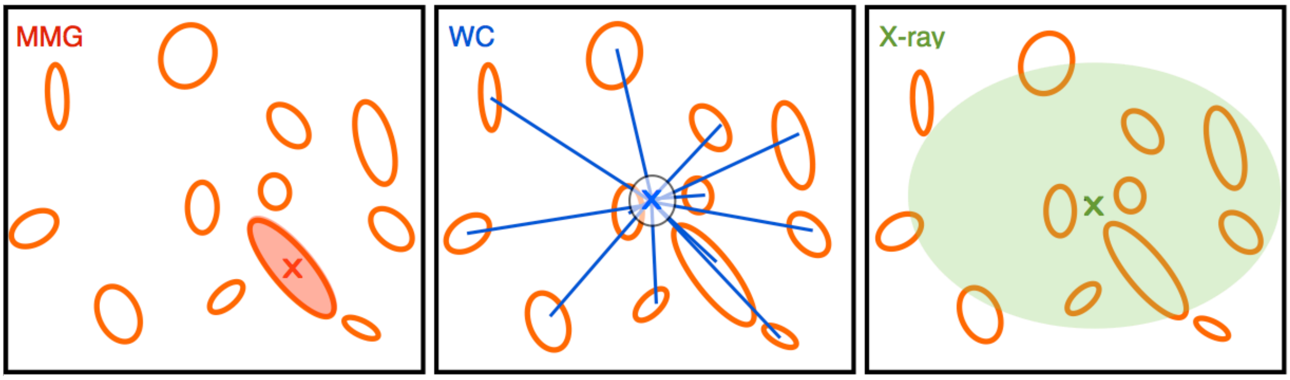

Figure 3.3: Illustration of the three different centre definitions. The orange symbols represent the galaxy member of the group. The shaded galaxy member represents the most massive galaxy, the blue line converge to the galaxy mass' weighted centre and the green shaded area shows the X-ray emission (if observed). The x symbol is associated to the centre definition in each panel.

In this work, two different candidate centres are analyzed and compared: the most massive galaxy (MMG) location and the galaxies' mass weighted centre (WC). In addition, for the X-ray sample we can use an extra centre candidate: the X-ray density peak (X-ray). The centre definitions are illustrated in Figure 3.3. Note the completeness is very high for the massive galaxies so the mass-weighted centre is well determined. The WC co-ordinate is computed by:

$$X = \frac{\sum x_i * m_i}{\sum m_i} \tag{3.2}$$

where x_i is the pair of coordinates (RA, DEC, Z) and m_i is the stellar mass.

Using the MMG location as the definition of the centre provides the opportunity to test the validity of the CGP. In such analysis it is important to properly identification the MMG.

Measurement uncertainties are a source of error in the estimation of stellar mass hence may cause the misidentification of the most massive galaxy. Furthermore, even though the most luminous galaxy is usually also the most massive galaxy it is not always the case. Missing members, due to redshift incompleteness, may also cause the misidentification of the most massive galaxy. In the aim of avoiding contamination from misidentification in our sample, we flag groups with the possibility of missing the brightest galaxy. For galaxies with missing spectroscopic redshifts, we use photometric redshifts (if available) estimated using the Hyperz4 code (Bolzonella et al., 2000) which generates redshifts through a standard SED fitting procedure from the available broad-band photometry. The accuracy of this technique was tested by comparing the photometric redshifts to the spectroscopic redshifts for galaxies with measured spectroscopic redshifts. Galaxies, with a photometric redshift including the possibility of being a member of a group, are flagged. We evaluate galaxies up to 0.5 R_{200} for the WC and the MMG. If these galaxies are brighter than the BHG and have a magnitude larger than -23, then the group is removed from the sample. Few galaxies still have undefined photometric and spectroscopic redshifts. Assuming these galaxies are at the same redshift of a group, if they respect the previous brightness condition then they are also flagged. Every group with a flagged galaxy is identified in Table 3.4 and are removed from the selected sample (see Section 3.4).

3.4 The Sample

In this work, we consider the groups within the two patches (14h and 21h), where X-ray imaging and extensive follow-up spectroscopy are available. Our initial sample is composed of 84 distinct groups. Among these, 40 groups were spectroscopically identified and are referred to as *optical groups* and 53 groups were identified through their X-ray emission and are referred to as *X-ray groups*. Only nine of these X-ray groups were previously identified with the F-O-F algorithm. X-ray group detection generally identifies more massive, evolved and relaxed systems (Finoguenov et al., 2009). Groups with less than 3 members and with a velocity dispersion higher than 1000 km/s were removed from the sample. After flagging groups with

Table 3.1: List of incomplete groups

Sample	Patch	Group ID [a]
X-ray	2148	06
X-ray	2148	14
X-ray	2148	37
X-ray	2148	49
Opt	1447	30
Opt	2148	111
Opt	2148	131
Opt	2148	138

---

[a] Group ID comes from Connelly et al. (2012)

possible misidentification of the MMG as discussed in the previous section, four groups have been removed in both samples (see Table 3.4). The complete sample is composed of 49 optically selected groups and 36 X-ray-selected group with seven groups which belong to both samples. In total 78 groups with secure MMGs are identified.

The sample spans a redshift range between ∼0.1-0.9, although the optical groups extend to only ∼0.55. Figure 3.4 shows the redshift distribution of the X-ray groups (in dashed green line) and of the optical groups (in solid magenta line).

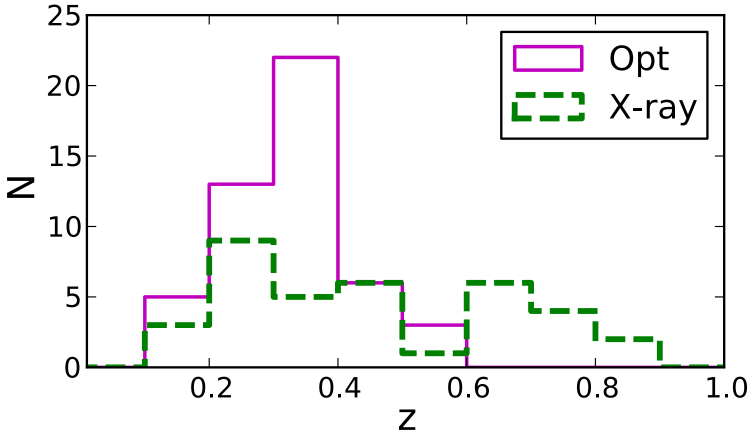

Figure 3.4: Redshift distribution for the X-ray and optical sample of the GEEC group catalog in dashed green line and solid magenta line, respectively.

We reproduced in Figure 3.5 the velocity dispersion and in Figure 3.6 the number of members per group versus the redshift for our selected groups where the X-ray groups are green squares and the optical groups are magenta circles. We note that, at high redshift, groups are biased towards systems with higher X-ray luminosity and higher velocity dispersion (hence higher mass). The mean velocity dispersions are 300 ± 163 km s^{-1} and 357 ± 230 km s^{-1} for the optical groups, and the X-ray groups respectively where the error represents the standard deviation. These values should be kept in mind when comparing the velocity dispersions obtained from our weak lensing analysis.

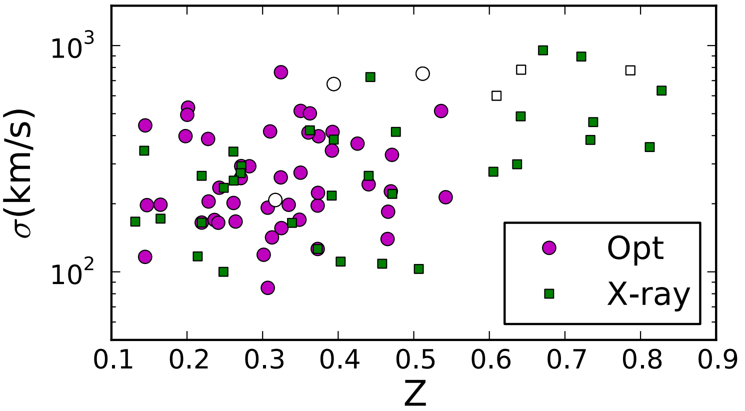

Figure 3.5: Velocity dispersion calculated with the Bergond moving window method versus redshift for X-ray groups (green squares) and for optical groups (magenta circles). The unfilled symbols represent groups that are classified as dynamically complex (see Section 3.4.2).

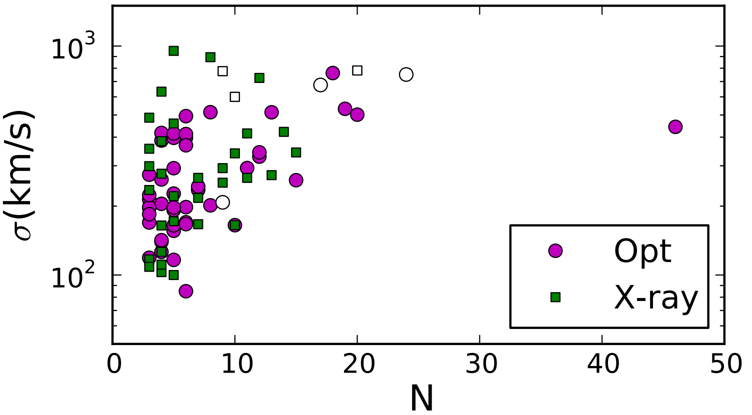

Figure 3.6: Velocity dispersion versus number of member per group for X-ray groups (green squares) and for optical groups (magenta circles). The filled magenta and green rectangles represent groups that are classified as dynamically complex (see Section 3.4.2).

In Figure 3.7, we can see the group size distribution of our sample. The size of the group (R_{200}) is defined as the virial radius (Carlberg et al., 2001). R_{200} is equal to the projected distance from the centre where the mean density inside that radius is equal to 200 times the critical density of the universe. The virial radius can be estimated as:

$$R_{200} = \frac{\sqrt{3}\sigma}{10H(z)} \tag{3.3}$$

where $H(z)$ is the Hubble constant and σ is the radial velocity dispersion. As we will see in Section 4, the size of the groups is a very important factor in weak lensing analysis as well as in the dynamical studies.

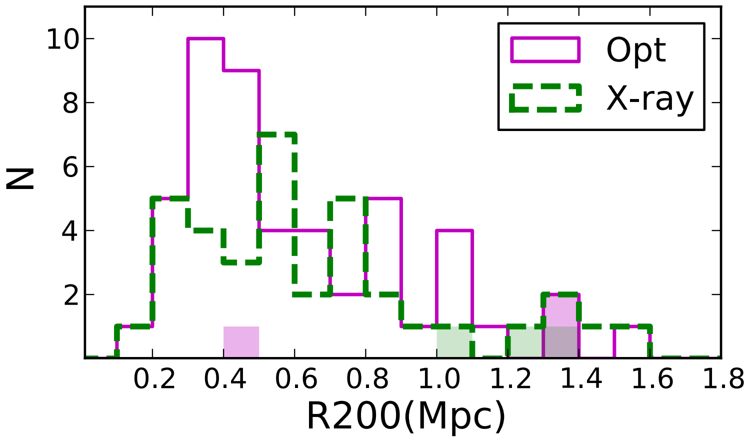

Figure 3.7: Histogram of the virial radius R_{200} in Mpc for the X-ray and optical samples in dashed green line and solid magenta line, respectively. The filled magenta and green rectangles represent groups that are classified as dynamically complex (see Section 3.4.2).

The halo mass distribution of our selected sample is shown in Figure 3.8. We calculate the mass using Equation 1.2 with the size distribution given in Figure 3.7. Our sample spans a mass range between $10^{12} - 10^{15} M_{\odot}$.

3.4.1 Offset between the candidate centres

As the offset between candidate centres affects the lensing signal profile, we compare in the top panel of Figure 3.9 the projected separation between the MMG and the WC candidate

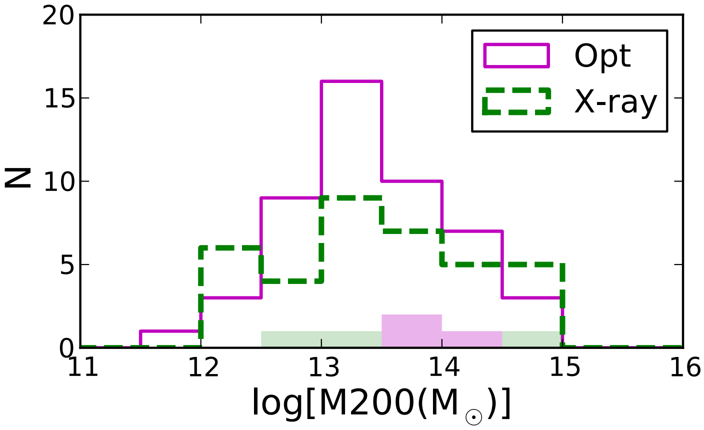

Figure 3.8: Distribution of the halo mass for X-ray groups (green squares) and for optical groups (magenta circles). The filled magenta and green rectangles represent groups that are classified as dynamically complex (see Section 3.4.2).

centres for the X-ray groups (in dashed green) and for the optical groups (in magenta). It is worth mentioning that the offset for the optically selected groups is slightly higher than for the X-ray selected groups which was previously reported in Connelly et al. (2012), where they used the luminosity weighted centre for the optical groups and the X-ray centre for the X-ray groups instead of the WC. From this observation, we expect the difference in the lensing signals for the optically selected groups to be more significant than for the X-ray groups. This hypothesis is addressed in Section 4.1.2. The bottom of Figure 3.2 represents the projected separation between the X-ray centre and the MMG (dashed red line) and between the X-ray centre and the WC (solid blue line) for the X-ray groups. We can see that the offset between the X-ray centre and the MMG is slightly higher than between the X-ray centre and WC. Hence we expect the disparity between the signals using the X-ray centre candidate and the signal using the MMG to be larger than using the WC candidate.

3.4.2 Dynamical Complexity

The calculation of the VDPs requires making the assumption that groups are in equilibrium, which may not be a valid assumption. In fact, galaxy groups may be significantly perturbed

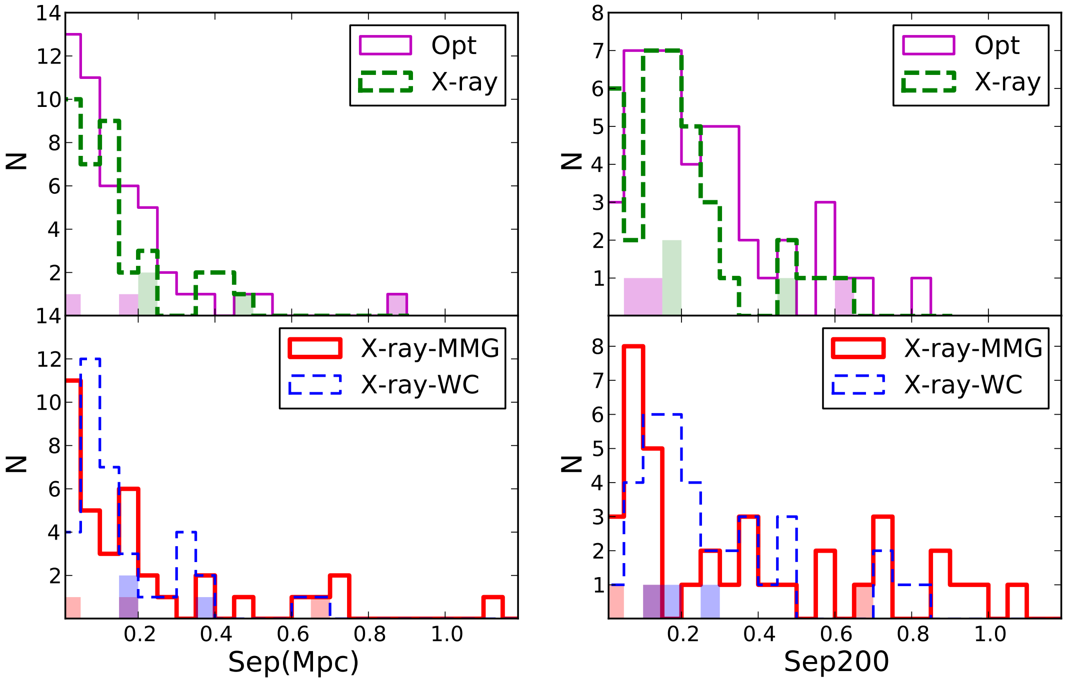

Figure 3.9: Histogram of the projected separation in Mpc (left panel) and in units of R_{200} (right panel) between the MMG and the WC for our sample. The distribution of optical and X-ray groups are shown in magenta solid line and green dashed-line respectively. The filled magenta and green rectangles represent groups that are classified as dynamically complex.

by mergers, accretion of subhalos or may be just forming. Merging systems and systems with substructure disturb the mass distribution of groups.

The impact of dynamical complexity on the weak lensing signal and VDP is examined in this thesis. As has been shown in Hou et al. (2009) the dynamical state of groups greatly influences the shape of a group's VDP. Groups in equilibrium either have a flat or generally decreasing profiles while dynamically complex groups have rising profiles (see Figure 3.10). For this reason, it becomes important to restrict our sample to dynamically evolved groups in order to be able to interpret our stacked VDP.

Although group dynamics play an important role in understanding the evolution of groups, relatively few studies on the dynamical state of groups have been done. Now, with the available large statistical samples of groups, it has been possible to develop and test reliable statistical tools to evaluate group dynamics. The dynamic complexity in groups can be studied using

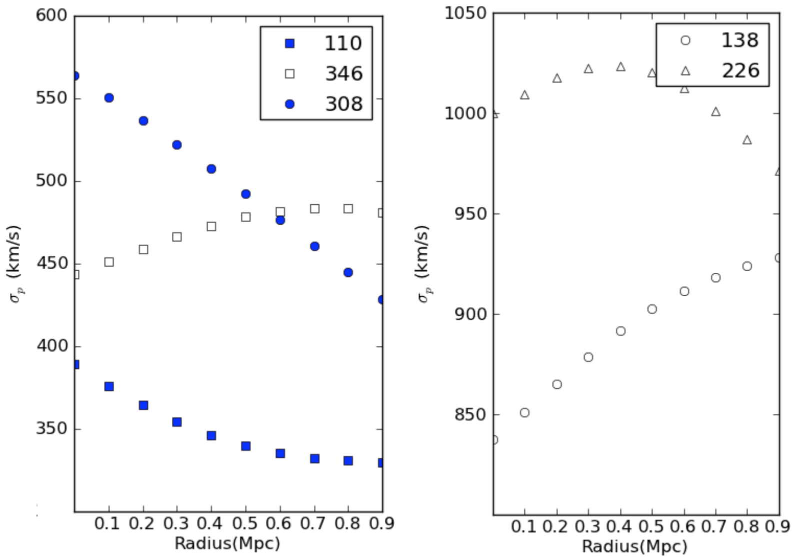

Figure 3.10: Adapted from Hou et al. (2009) Velocity dispersion profiles for five groups from the GEEC catalog where the group ID are identified in the legend. The open symbols indicate group that are classified as complex and the closed symbols indicate those that are classified as non-complex.

a one-dimension (1-D) test, a three-dimension (3-D) test or the VDP. Those techniques have been studied in detail in Hou et al. (2009, 2012). The 1-D test is based on the assumption that, for a group in dynamical equilibrium, the radial velocity distribution is expected to take a Gaussian shape as illustrated in Figure 3.11. Note, this standard assumption is not strictly true if the system is not in dynamical equilibrium. By comparing different statistics such as the Kolmogorov-Smirnov (KS) test, the Pearson's χ^2 Test and the Anderson-Darling (AD) test, Hou et al. (2009) concluded that the AD test is the best test to determine whether a small sample size is drawn from a Gaussian distribution. By comparing the VDP for groups classified as Gaussian (closed symbols of Figure 3.10) and non-Gaussian (open symbols of Figure 3.10), one can see that non-Gaussian groups have rising profiles while Gaussian groups have decreasing profiles. According to Hou et al. (2009), $\sim 32\%$ of the optical GEEC groups had non-Gaussian velocity distributions.

An alternative way to investigate galaxy group dynamics uses the positions and radial velocities of member galaxies to look for substructure in the systems. Such 3-D tests have been

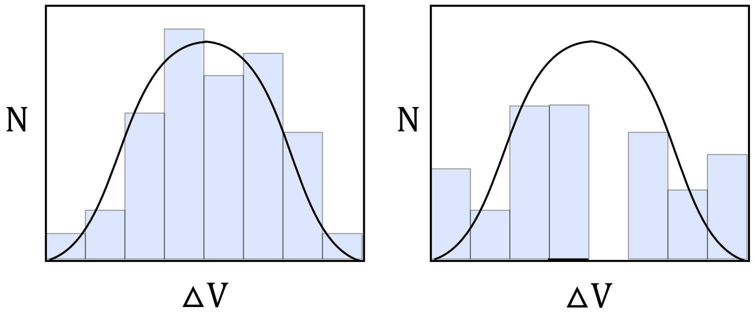

Figure 3.11: Radial velocities distribution in a group which classified as a Gaussian (right), classified as non-Gaussian (left).

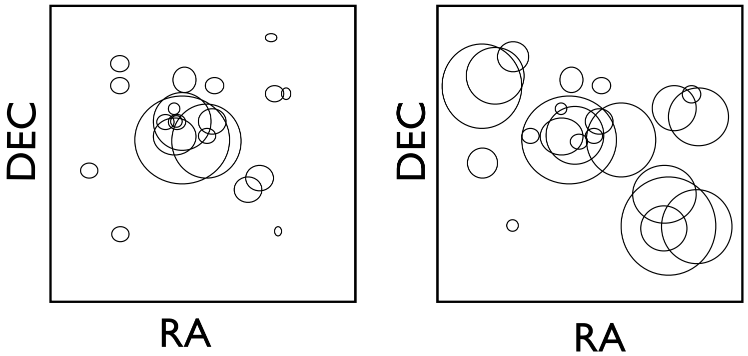

Figure 3.12: Bubble diagram of the Dressler & Shectman (1988) structure test where the galaxy symbols scale the galaxy deviation of the local velocity mean and of the group velocity dispersion. The left panel represents a group without substructure the right panel represents the group with substructure.

widely used in galaxy cluster studies, but require a large number of members per system and so have not been widely applied to groups. The most common such test is the Dressler-Shectman (hereafter DS, Dressler & Shectman, 1988) which has been adapted to group-size halos. This test identifies clumps of galaxies which have different dynamical properties than the host halo such. The presence of substructure in groups and clusters highly suggests that the system is in the procress assembling or accreting galaxies or small systems (see Figure 3.12).

These two statistical tests were applied for the GEEC group catalog in Connelly et al. (2012). Six X-ray groups and five optical groups were identified as complex according to AD or DS tests (see Table 3.4.2). Note that three of the X-ray groups and one of the optical groups were already removed previously due to incompleteness issues (see Table 3.4). Four groups identified as complex were removed in our optical sample and three groups were removed in

Table 3.2: List of complex groups

Sample	Patch	Group ID [a]	Dynamical Complexity
X-ray	1447	09	AD,DS
X-ray	1447	03	AD
X-ray	1447	44	AD,DS
X-ray	2148	14	AD
X-ray	2148	37	AD,DS
X-ray	2148	49	AD
Opt	1447	32	DS
Opt	1447	37	AD
Opt	1447	38	AD
Opt	2148	129	AD
Opt	2148	138	AD

---

[a] Group ID comes from Connelly et al. (2012)

the X-ray sample. These groups are identified in Figure 3.5 and 3.6 in unfilled symbols, and in Figure 3.7 and Figure 3.8 in shaded rectangles. We note that these groups are relatively large, massive and at high redshift. Finally, 45 optical and 33 X-ray groups remain after deleting groups with dynamical complexity or substructure.

Bibliography

Balogh, M. L., Wilman, D., Henderson, R. D. E., et al. 2007, MNRAS, 374, 1169

Balogh, M. L., McGee, S. L., Wilman, D., et al. 2009, MNRAS, 398, 754

Balogh, M. L., McGee, S. L., Wilman, D. J., et al. 2011, MNRAS, 412, 2303

Beers, T. C., Flynn, K., & Gebhardt, K. 1990, AJ, 100, 32

Bolzonella, M., Miralles, J.-M., & Pelló, R. 2000, A&A, 363, 476

Bruzual, G., & Charlot, S. 2003, MNRAS, 344, 1000

Carlberg, R. G., Yee, H. K. C., Morris, S. L., et al. 2001, ApJ, 552, 427

Chabrier, G. 2003, PASP, 115, 763

Connelly, J. L., Wilman, D. J., Finoguenov, A., et al. 2012, ApJ, 756, 139

Dressler, A., & Shectman, S. A. 1988, AJ, 95, 985

Finoguenov, A., Connelly, J. L., Parker, L. C., et al. 2009, ApJ, 704, 564

Hou, A., Parker, L. C., Harris, W. E., & Wilman, D. J. 2009, ApJ, 702, 1199

Hou, A., Parker, L. C., Wilman, D. J., et al. 2012, MNRAS, 421, 3594

Huchra, J. P., & Geller, M. J. 1982, ApJ, 257, 423

Le Fevre, O., Crampton, D., Felenbok, P., & Monnet, G. 1994, A&A, 282, 325

McGee, S. L., Balogh, M. L., Wilman, D. J., et al. 2011, MNRAS, 413, 996

Parker, L. C., Hudson, M. J., Carlberg, R. G., & Hoekstra, H. 2005, ApJ, 634, 806

Wilman, D. J., Balogh, M. L., Bower, R. G., et al. 2005, MNRAS, 358, 71

Wilman, D. J., Pierini, D., Tyler, K., et al. 2008, ApJ, 680, 1009

Wilman, D. J., Oemler, A., Jr., Mulchaey, J. S., et al. 2009, ApJ, 692, 298

Yee, H. K. C., Morris, S. L., Lin, H., et al. 2000, ApJS, 129, 475

Chapter 4

Results

We present the results of the weak lensing analysis in Section 4.1 and the dynamics analysis results in Section 4.2.

4.1 Weak Lensing

4.1.1 Entire Sample

The tangential shear profiles for the GEEC selected groups are illustrated in Figure 4.1. As previously mentioned, our sample spans a wide range of sizes (see Figure 3.7). Therefore, the signals around smaller groups are overwhelmed by the signals of the larger groups. To overcome this problem, we normalize the projected distance between the lens-source pairs by the size of the group (R_{200}). The lensing signal for the weighted centre (WC) definition is shown in blue while the lensing around the MMG is shown in red. We select a bin width of 0.4 R/R_{200}. This choice of binning provides reasonably small uncertainties for each bin. We evaluate the tangential shear up to $2.4R/R_{200}$. This scale corresponds to a mean physical scale of $\sim$2.3 Mpc since the mean value of R_{200} is ~ 0.9 Mpc. This limit is well justified as it represents more than two times the size of each group and one does not expect significant signal at this distance. We remove lens-source pairs within 7" from the MMG position since its light may interfere with the shape measurement of the sources. In order to fit our data to dark matter halo models, the distance of the source (D_S) needs to be known (see Section 2.2.3). However, the spectroscopic survey was not designed to determine deep redshifts of faint distant galaxies and only half of the sources have high quality photometric redshifts. If one knows the redshift distribution of the sources, the knowledge of their individual redshifts is not critical. We use the median value from the photometric redshift distribution, z=0.9, found in Parker et al. (2005).

We fit our data with the SIS profile (solid line) and the NFW (dashed line) profile. We fix the value of the concentration c in the NFW fitting to 10. This assumption is well justified for the group scale (Bullock et al., 2001). As we are interested in relative lensing measurements between different centre definitions, and the two models (the SIS and NFW) cannot be differentiated with our data, we select only the SIS model for the remainder of the thesis. This model selection will also allow us to compare to previous results (Parker et al., 2005; Finoguenov et al., 2009). The 1-sigma contour is represented by the shaded area for the SIS profile. The best fit parameter has been found using the least squares curve fitting:

$$\chi^2 = \sum_i \frac{\gamma_{\mathrm{Data}}(R/R_{200,i}) - \gamma_{\mathrm{Model}}(R/R_{200,i})}{\sigma_i^2} \tag{4.1}$$

where σ_i is the measurement of the uncertainty on $\gamma_{\mathrm{Data}}(R/R_{200,i})$. Our fitting is done with a curve fitting package in python which uses the Levenberg-Marquardt algorithm. This damping algorithm is convenient as it can find a solution even if the initial hypothesis is very far off the final minimum.

We evaluate which of the WC and MMG candidate centres best trace the underlying matter distribution. From the top panel of Figure 4.1, it appears that the WC is a better definition of the centre for our group sample as it reaches higher values on small scales than the MMG definition. As the signal vanishes at large scales, we focus our attention in the inner part of the profile. By evaluating the tangential shear within the group virial radius, we compare the amplitude of the shear. The ratio of the signal using the MMG candidate and the WC candidate is $\langle\gamma_t\rangle_{\mathrm{R200,MMG}}/\langle\gamma_t\rangle_{\mathrm{R200,WC}} \sim$0.71. The ratios from the tangential shear measurement within R_{200} are shown in Table 4.1 This result is not in agreement with what has been found by George et al. (2012). This contradiction is discussed in Chapter 5. It is worth mentioning that the analysis by George et al. (2012) was done on a X-ray group sample while our sample

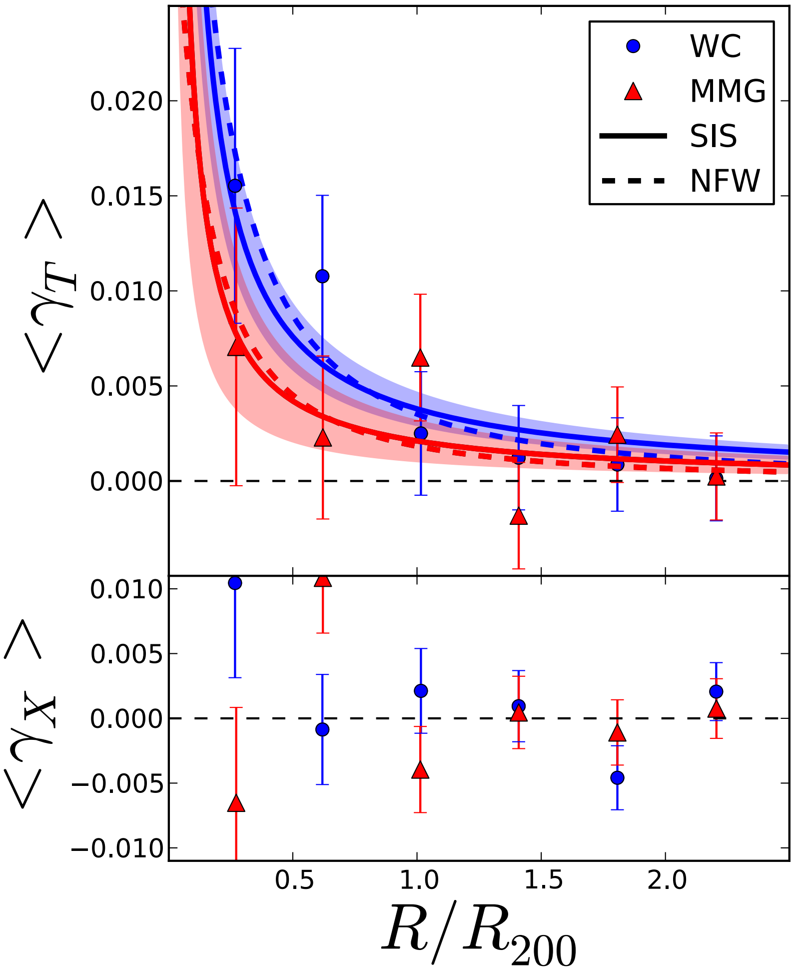

Figure 4.1: Average tangential shear (top panel) and cross-shear (bottom panel) as a function of the radius in units of R_{200} around 78 galaxy groups from GEEC catalog for the WC candidate centre (blue circles) and the MMG candidate centre (red triangles). The error bars represent the statistical uncertainty.

is mostly composed of optically selected groups. In the next section, we examine the difference in the shear signals from the X-ray selected and optically selected groups in order to evaluate the impact of optical groups in our signal.

The bottom panel of Figure 4.1 represents the cross-shear signal (see bottom panel of Figure 2.7) which is a direct way to test if our signal is caused by gravitational lensing. By rotating the position of the background galaxies by a factor of 90° around the lens centre without changing their orientation, the lensing signal should vanish. As shown in the bottom of Figure 4.1, our cross-shear signal scatters around zero with an uncertainty consistent with a zero signal. We also measure the lensing signal by randomly relocating the position of the groups and the signal is still consistent with a null signal suggesting that our lensing signal is real.

From the lensing method, we extract the averaged velocity dispersion, $\sigma_{\rm len}$, of the selected GEEC groups. We did not normalize the projected distance in the evaluation of the velocity dispersion to ensure that our results are independent of the dynamical estimation of R_{200}. The velocity dispersion is obtained by evaluating the shear up to 200" with a binning of 50". The SIS fitting gives us the following results $\sigma_{\rm len,MMG} = 157 \pm 53$ km s^{-1} and $\sigma_{\rm len,WC} = 255 \pm 38$ km s^{-1}.

As we already mentioned in Section 3.1, the velocity dispersions of the X-ray and optical GEEC catalog were previously calculated in Connelly et al. (2012) using the radial velocities of member galaxies, assuming different definitions for the size of the group (note that σ depends on the radius). In the thesis, we focus on the intrinsic velocity derived from the $R_{200,\sigma}$ cut[1], where $R_{200,\sigma}$ is the virial radius defined as in Equation 3.3. Thus, every member with a projected distance larger than the virial radius is not considered in the evaluation of the velocity dispersion. We compare the velocity dispersions ($\sigma_{\rm len}$) obtained from our SIS fitting with the those from Connelly et al. referred to as the dynamical velocity dispersion $\sigma_{\rm dyn}$. We do not simply calculate the mean dynamical velocity dispersion for the sample, as previously done in Section 3.4. When calculating the tangential shear, we also weight the velocity dispersion

---

[1] available in Table 4 and 6 of Connelly et al. (2012).

Table 4.1: Ratio of the lensing signal within R_{200}

Sample	$\langle\gamma_t\rangle_{\rm MMG}/\langle\gamma_t\rangle_{\rm WC}$	$\langle\gamma_t\rangle_{\rm MMG}/\langle\gamma_t\rangle_{\rm X\text{-}ray}$	$\langle\gamma_t\rangle_{\rm WC}/\langle\gamma_t\rangle_{\rm X\text{-}ray}$
All groups	0.71	-	-
Optical.........	0.49	-	-
X-Ray..........	0.78	0.47	0.60
Evolved Systems:			
Optical........	0.62	-	-
X-Ray.........	0.76	0.4	0.52

Table 4.2: Velocity Dispersion (in km s^{-1}) from Weak Lensing and Dynamical Methods

Sample	$\langle\sigma\rangle_{\rm MMG,len}$	$\langle\sigma\rangle_{\rm WC,len}$	$\langle\sigma\rangle_{\rm X\text{-}ray,len}$	$\langle\sigma\rangle_{\rm dyn}$	$\langle\sigma\rangle_{\rm Fin.}$ [a]
All groups....	157±53	255±38	-	318±221	-
Optical.........	118±98	224±38	-	269±138	228±137
X-Ray..........	169±82	271±63	339±50	352±149	309±106
Evolved Systems:					
Optical........	143±84	215±46	-	238±142	-
X-Ray.........	111±156	201±98	302±54	316±150	-

---

[a] Velocity dispersion measured from weak lensing in Finoguenov et al. (2009)

and uncertainties as in Equation 2.8. Therefore, the mean dynamical velocity dispersion is weighted by the number of lens-source pairs from the weak lensing method which provides us a fair comparison between both results. We find a mean dynamical velocity dispersion of $\sigma_{\rm dyn} = 318 \pm 221$ km s^{-1}. The results from both techniques can be found in Table 4.2. The dynamical method gives results that are higher than with the weak lensing method. It is possible that the velocity dispersion gives an overestimation of the real value in groups due to the small statistics in groups.

4.1.2 X-ray and optical groups shear

In this section, we compare the weak lensing properties of the spectroscopically selected sample and the X-ray-selected sample. The optical and X-ray samples are composed of 49 and 36 groups respectively. We evaluate the stacked lensing signal for the optically selected groups using the previous centre definitions: WC (in blue) and MMG (in red). For the X-ray groups, an additional centre is considered: the X-ray centre (in green).

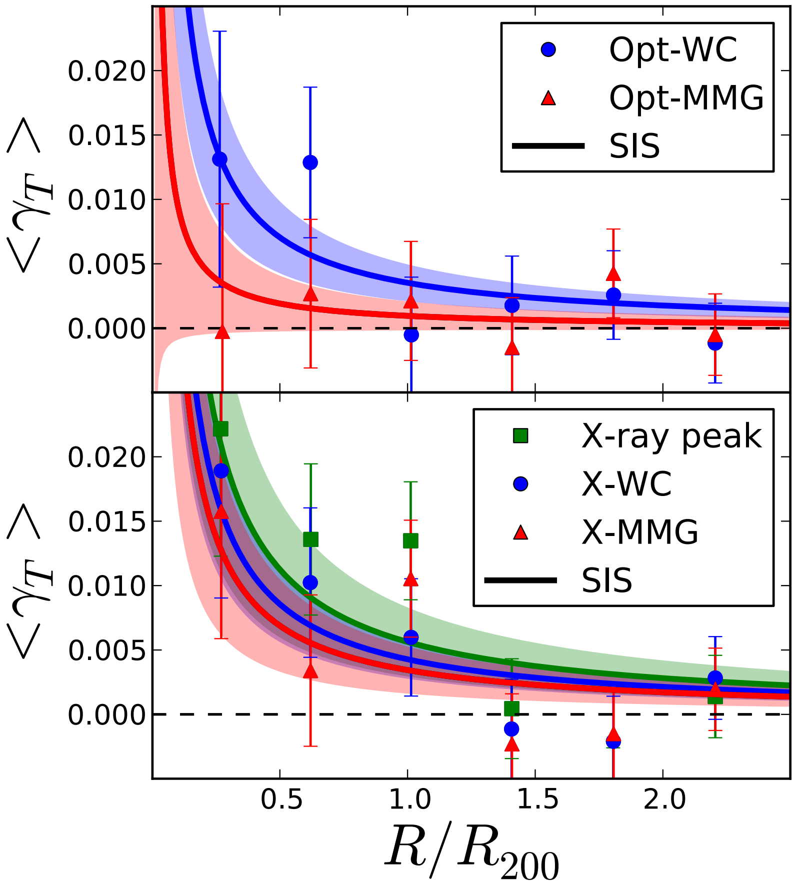

Figure 4.2: Average tangential shear for the optical group (top panel) and the X-ray groups (bottom panel) for the WC candidate centre (blue circles), the MMG candidate centre (red triangles) and the X-ray centre (green square).

The lensing signals for the two samples are shown in Figure 4.2 where the top panel represents the optical group signals and the bottom panel represents the X-ray group signals. The optical group signal reaches a higher maximal value when using the WC definition than the MMG definition. Note that we do not get a statistically significant detection from the MMG candidate. Our findings indicate that the WC seems to be the best definition of the centre for the optical groups. On the other hand, for the X-ray groups, the choice of centre definition does not significantly influence the shear signal. The X-ray centre definition gives slightly higher signal than the WC and the MMG definition. We can calculate teh ratio of the mean shear within the virial radius for different centre definitions. For the optical groups, we find the following ratio $\langle\gamma_t\rangle_{\mathrm{R200,MMG}}/\langle\gamma_t\rangle_{\mathrm{R200,WC}}$ $\sim$0.49. For the X-ray groups, we find $\langle\gamma_t\rangle_{\mathrm{R200,MMG}}/\langle\gamma_t\rangle_{\mathrm{R200,X\text{-}Ray}}$ $\sim$0.47 for the MMG and the X-ray centre definitions, $\langle\gamma_t\rangle_{\mathrm{R200,MMG}}/\langle\gamma_t\rangle_{\mathrm{R200,WC}}$ $\sim$0.78 for the MMG and WC centre definitions and $\langle\gamma_t\rangle_{\mathrm{R200,WC}}/\langle\gamma_t\rangle_{\mathrm{R200,X\text{-}Ray}}$ $\sim$0.60 for the WC and X-ray centre definitions. Note that all of these ratios have large uncertainties as the uncertainties on the signal are $\sim$ 30% for the X-ray centre definition and $\sim$ 50% for the MMG and WC definitions.

For the weak lensing signal evaluated within 200", the average velocity dispersions for the selected GEEC sample, using the SIS fitting, are $\sigma_{\mathrm{len,WC}} = 224 \pm 38$ km s^{-1} and $\sigma_{\mathrm{len,MMG}} = 118 \pm 98$ km s^{-1} for the optical groups. For the X-ray groups, we obtain $\sigma_{\mathrm{len,WC}} = 271 \pm 63$ km s^{-1}, $\sigma_{\mathrm{len,MMG}} = 169 \pm 82$ km s^{-1} and $\sigma_{\mathrm{len,X\text{-}ray}} = 339 \pm 50$ km s^{-1}.

The main velocity dispersions obtained with Connelly et al. estimations are $\sigma_{\mathrm{dyn}} = 269 \pm 138$ km s^{-1} for the optical groups. For the X-ray groups, we find $\sigma_{\mathrm{dyn}} = 352 \pm 149$ km s^{-1}. These weighted values are consistent with the mean velocity dispersion calculated in Section 3.4 for both samples. The lensing and dynamical methods give similar results, only the MMG candidate in the optical provides lower estimation. The X-ray and the WC definitions give the best agreement between both methods.

The velocity dispersions obtained from the lensing and dynamical methods are in agreement with previous work by Finoguenov et al. (2009) who estimated the velocity dispersion using the same basic sample. They used the X-ray centre for the X-ray sample and the luminosity weighted centre for the optical groups which can be fairly compared to $\sigma_{\mathrm{len,WC}}$. From the weak lensing signal around spectroscopically selected groups within the 14h & 21h CNOC2 field, they obtained $\sigma_{\mathrm{opt}} = 228 \pm 137$ km s^{-1}. They also evaluate the lensing signal for the X-ray detected groups with redshift and obtained $\sigma_{\text{X-ray}} = 309 \pm 106$ km s^{-1}. The comparison of the X-ray and optical groups signals clearly indicates that the full stacked signal (see Figure 4.1) is dominated by X-ray groups for the MMG candidate. Furthermore, the signals for the X-ray groups are consistently independent of the centre definition while for the optical groups the WC is a better definition than the MMG position.

4.1.3 Evolved Sample

In this section, we explore the effects of groups with dynamical complexity on our lensing measurement where complex groups were identified in Section 3.4.2. For dynamically unevolved groups their mass profiles are not well fit by the standard model and the interpretation of the lensing signal may be more complicated. Due to the low number of observable members in groups, statistical tests to search for merging and substructure which are used in clusters may be inefficient. The weak lensing method provides an opportunity to verify the validity of such tests.

The average tangential shear around 45 optical and 33 X-ray groups without dynamical complexity are shown in Figure 4.3. The average tangential shear for the X-ray groups remains similar to the previous analysis shown in Figure 4.1. However, for the optical sample, the signal for the MMG candidate is better. The previous signal of the optically selected systems was significantly affected by a few dynamically complex groups (see Figure 4.2). For the X-ray systems, the presence of a few dynamically complex groups did not have as much influence on the signal in our sample. Our findings indicate that the dynamical complexity in groups cannot be neglected as it may considerably diminish the lensing signal.

Our findings on evolved groups gives a ratio of $\langle\gamma_t\rangle_{\mathrm{R200,MMG}}/\langle\gamma_t\rangle_{\mathrm{R200,WC}}$ ~0.62 for the optical groups. For the X-ray groups, we have $\langle\gamma_t\rangle_{\mathrm{R200,MMG}}/\langle\gamma_t\rangle_{\text{R200,X-Ray}}$ ~0.4 for the MMG and X-ray

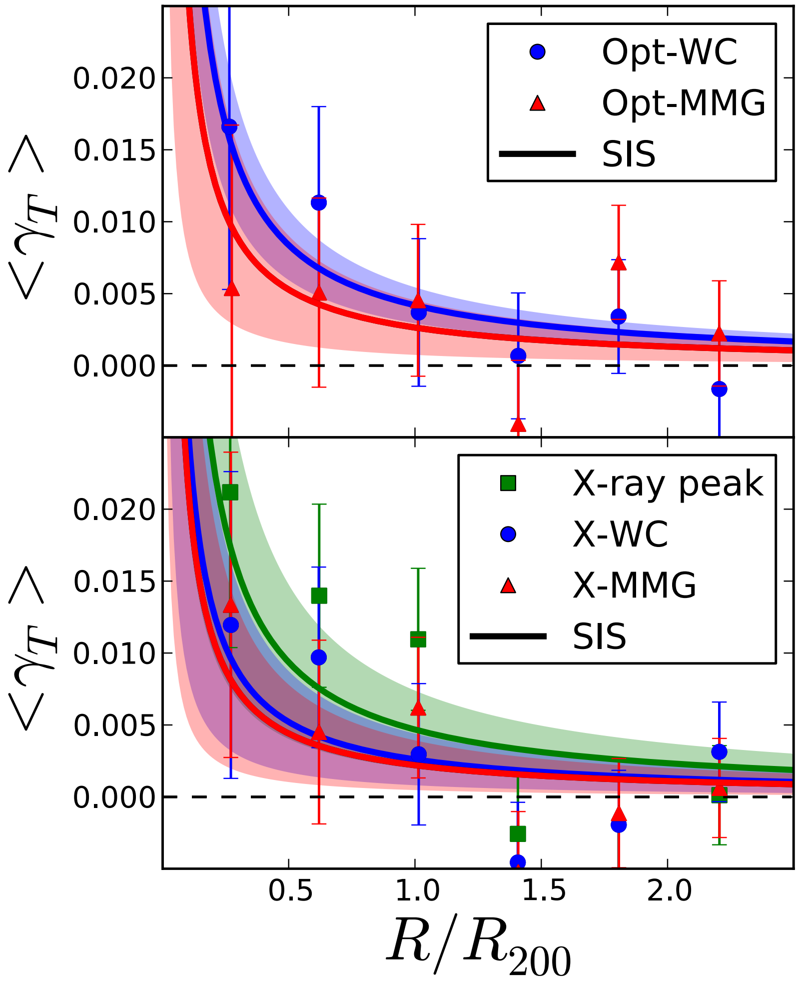

Figure 4.3: Tangential shear for the optical group (top panel) and the X-ray groups (bottom panel) where the WC candidate centre are in blue circles, the MMG candidate centre are in red triangles, and the X-ray centre is in green squares. The groups classified as dynamically complex have been removed from the sample.

candidate centres, $\langle\gamma_t\rangle_{\mathrm{R200,MMG}}/\langle\gamma_t\rangle_{\mathrm{R200,WC}}$ ~0.76 for the MMG and WC candidate centres and $\langle\gamma_t\rangle_{\mathrm{R200,WC}}/\langle\gamma_t\rangle_{\mathrm{R200,X\text{-}Ray}}$ ~0.52 for the WC and X-ray candidate centres. The conclusion for the X-ray groups remains the same; the lensing signal around evolved groups is not affected by the choice of MMG or WC definition and the X-ray centre definition seems better at tracing the mass distribution of the dark matter halo. For the optical groups, the WC gives a slightly stronger signal than the MMG. However, the lensing signals from the two centre definitions are in much better agreement than when the dynamically complex groups were included in the sample.

The velocity dispersion obtained from the weak lensing signal and the dynamical method can be found in Table 4.2. For the X-ray groups, the X-ray definition gives the best agreement for both techniques, while the WC definition gives more consistent results than the MMG definition in both sample.

In summary, although the S/N is low, the weak lensing signal around optical groups indicates that the WC is the best centre definition. However, the difference between the MMG and WC vanishes when dynamically complex groups are removed from the sample. For X-ray groups, we note that our signals are slightly in favour of the X-ray centre but there is no obvious best centre definition.

4.2 Dynamical Results

In this section, we investigate the difference between the stacked VDP for groups using the WC and the MMG centre definitions (see Figure 4.4). This analysis provides the opportunity to evaluate which definition is closer to the centre of potential in groups.

In the same manner as in the weak lensing analysis, we normalize the distance axis by the size of the group in order to account for the size of each group. The VDP has been evaluated up to one R/R_{200} which corresponds to the membership boundary. Additionally, we normalize the velocity dispersion σ_p by the intrinsic velocity dispersion of the groups σ_{int} defined in

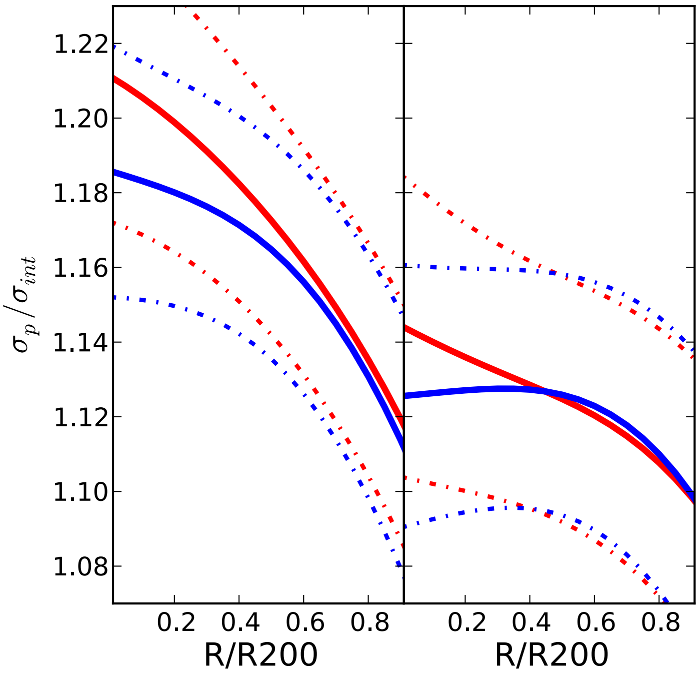

Figure 4.4: Normalized VDP using Bergond method for the entire sample (left panel) and around the evolved systems (right panel) where the blue line is obtained using the WC definition and the red line is obtained using the MMG definition. The uncertainty is represented in dashed-dot line.

Connelly et al. (2012). Note, the VDP is based on a simple standard deviation equation while the intrinsic dispersion has been estimated from a more sophisticated algorithm: the Gapper algorithm. Therefore, the standard deviation tends to overestimate the velocity dispersion of the groups. For this reason, the normalized VDP reaches values higher than 1. The VDP has been evaluated for the satellite galaxies only (we remove the MMG from the sample). Roughly 500 satellites in each group sample galaxies are available. In total, ~1000 tracers are used in the measurement of the VDP.

We show, in the left panel of Figure 4.4, the stacked VDP of the entire sample using the WC as the centre of the groups in blue and using the MMG as the centre of the groups in red. The dashed line represent the uncertainty, which has been determined by using the Jackknife method which is an accurate algorithm for small samples. Figure 4.4 shows that the MMG reaches slightly higher values at small scales. Nevertheless, once we consider the uncertainty, both profiles are overlapping. With our sample there is no statistically significant difference in the VDPs for the two definitions of group centres.

As discussed in Section 3.4.2, the study of recently formed groups or groups currently undergoing mergers can be complicated by their non-Gaussian velocity distributions. The VDP of complex groups may exhibit different features from unrelaxed systems. Hence, we remove the dynamically complex groups from our sample and examine the effect of this cut on our VDP. The right panel of Figure 4.4 represents the VDP of evolved groups. The profile is closer to 1 indicating that the groups with overestimated velocity dispersions have been removed from the sample. The VDP is not as steep but it is still in favour of the MMG definition, Nevertheless, the uncertainties are too large to confirm this observation.

Although the uncertainties over the entire sample are large, we still evaluate the VDP around X-ray and optical groups (see left panel of Figure 4.5) separately in order to extract as much information about our two samples. For the optical groups, the MMG seems to be a better assumption of the centre than the WC, while for the X-ray groups there is no obvious distinction between the two candidates.

Once we remove the unevolved systems from the two samples, we recomputed the VDPs as shown in the right panel of Figure 4.5. The signals are not as steep, which is consistent with Figure 4.4. The optical group VDP using the MMG centre definition is still rising up towards the centre. On the other hand, for the X-ray groups, the WC definition is better at tracing the centre than the MMG definition. Due to the large uncertainties, we cannot conclude which centre definition is better at tracing the potential centre as more groups need to be added to the sample. Nevertheless, by comparing the VDPs from Figure 4.5 to those from Figure 4.4, one can observe an interesting point. We note that the rising feature towards the centre using the MMG definition is mostly dominated by the optical groups.

An alternative way to evaluate if our centre definitions are offset with the real centre is to look at the surface density profile which represents the number of members per area, as shown in Figure 4.6. We used the surface density function defined in Wright & Brainerd (2000) to fit

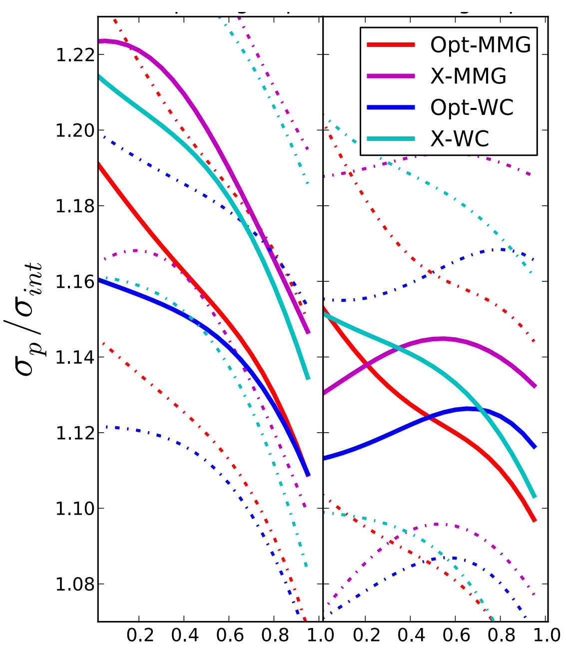

Figure 4.5: Normalized VDP using Bergond method around X-ray and optical groups (left panel) and around the evolved X-ray and optical groups (right panel) where the blue and cyan lines are obtained using the WC definition for the optical and X-ray groups respectively, and the red and magenta lines are obtained using the MMG definition for the optical and X-ray groups respectively. The uncertainty is represented in dashed-dot line.

our data. The MMG has not been removed from the sample in the evaluation of the surface density profile. The WC reaches higher values at small scales and as we expect the density profiles in groups to increase toward the centre, the WC seems closer to the real centre than the MMG. However, it is worth noting that the surface density profile is very sensitive to the spatial completeness. As the galaxy density increases toward the group centre, missing galaxy spectra identification (due to high densities) constitute a major issue in the surface density analysis.

From the distribution given in Figure 4.6, we construct fake groups which replicate the size, number of members and velocity dispersion of our group sample. We redistribute the position of the members to fit a perfect Gaussian velocity distribution. From this simulated sample, we recalculate the VDP 100 times and show the averaged VDP in Figure 4.7. The error bar represents the standard deviation of each bin. The red profile is associated with the MMG surface density profile while the blue profile is obtained from the WC surface density profile.

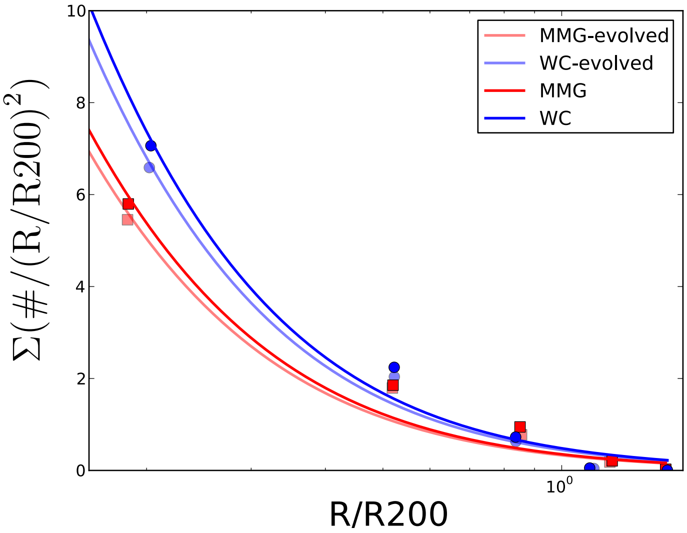

Figure 4.6: Surface density of the members as a function of the distance in units of R_{200} for the MMG candidate (in red) and the WC candidate (in blue) where the evolved samples are represented in shaded lines.

Assuming our group sample is drawn from a perfect velocity distribution, one would expect the WC to reach slightly higher values at small scales than the MMG for the surface density distribution given in Figure 4.6. We impose arbitrary offsets to the position of the centre and see the influence of the VDPs. In Figure 4.7, we show an example of VDPs with an offset of 0.0004° which is equivalent to ∼10 kpc in cyan for the WC definition and in magenta for the MMG definition. As we can see with an offset of ∼10 kpc, the VDPs are significantly influenced and tend to flatten.

Contrary to the weak lensing results, the dynamical results, for the optical groups, do not favour the WC definition. Nevertheless, the uncertainties on the VDP are too large to detect a significant distinction between the MMG and WC definition. More groups need to be added to the sample in order to reduce the uncertainties. On the other hand, the surface density profiles of the selected GEEC group suggest that the WC is closer to the real centre although we are aware that the distributions suffer from high membership incompleteness toward the centre.

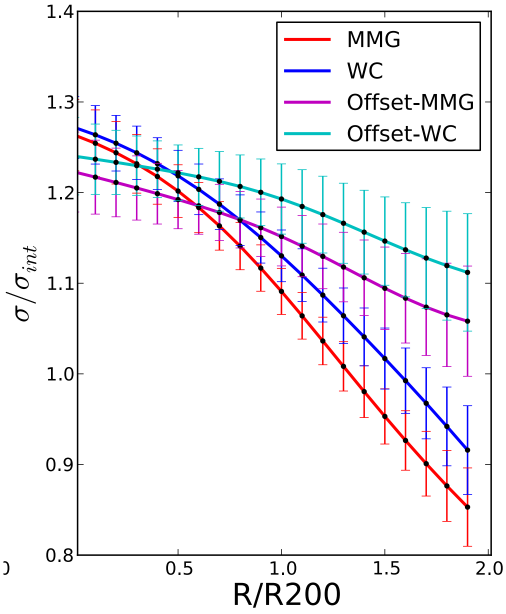

Figure 4.7: Averaged over 100 reconstructions of the VDP from the WC surface density profile (in blue) and the MMG surface density profile (in red). Averaged reconstructed VDP with an offset of 0.0004° (∼10 kpc) for the MMG surface density profile (in cyan) and and for the WC surface density profile (in magenta).

Bibliography

Bullock, J. S., Kolatt, T. S., Sigad, Y., et al. 2001, MNRAS, 321, 559

Connelly, J. L., Wilman, D. J., Finoguenov, A., et al. 2012, ApJ, 756, 139

George, M. R., Leauthaud, A., Bundy, K., et al. 2012, ApJ, 757, 2

Finoguenov, A., Connelly, J. L., Parker, L. C., et al. 2009, ApJ, 704, 564

Parker, L. C., Hudson, M. J., Carlberg, R. G., & Hoekstra, H. 2005, ApJ, 634, 806

Parker, L. C., Hoekstra, H., Hudson, M. J., van Waerbeke, L., & Mellier, Y. 2007, ApJ, 669, 21

Wright, C. O., & Brainerd, T. G. 2000, ApJ, 534, 34

Chapter 5

Discussion and Conclusion

In this chapter, we discuss our results and compare our findings with the weak lensing results of George et al. (2012) in Section 5.1. Finally, we review our findings and give a brief conclusion of our work in Section 5.2.

5.1 Discussion

It is of great interest to compare our results with those of George et al. (2012). George et al. (2012) used a sample of 129 X-ray selected galaxy groups from the COSMOS field in the redshift range $0 < z < 1$. We illustrate their weak lensing measurements as white circles in Figure 5.1, where each panel represents a different centre candidate. In the top panel of Figure 5.1, the centre is defined as the position of the most massive galaxy within R_{200} (referred to as MMGG$_{R200}$ in their original paper). In the middle panel of Figure 5.1, the centre is defined as the galaxies' mass weighted centre (referred to as CM in their paper). In the bottom panel of Figure 5.1, the centre is defined as the X-ray centroid (referred to as X-ray in their paper). The shear is expressed in term of the excess surface density, $\Delta\Sigma(R)$, as in Equation 2.9, in order to compare our results with George et al. (2012). In contrast with the previous figures, the projected distance (expressed in physical units h_{72}^{-1}Mpc) has not been scaled to the groups' size. We change the binning to match the bin width used in George et al. (2012). The lensing measurement for our sample is: in red triangles using the MMG definition; in blue circles using the WC definition; and, in green using the X-ray centroid definition. We note that George et al. benefit from smaller uncertainty due to their larger sample.

We do not expect the amplitudes of the George et al. signals to be the same as in our signals as the samples are not the same. The amplitude of a signal is proportional to the mass of the sample and the sample used in George et al. (2012) spans a mass range between $10^{13} - 10^{14}\mathrm{M}_{\odot}$, which was found through the weak lensing method. Our sample spans a larger mass range of $10^{12} - 10^{15}\mathrm{M}_{\odot}$, which was found using the dynamical method. However, even if the amplitudes are different, the shape of both samples can be compared. Our shape profiles are mostly consistent with George et al. with the exception of the inner profile of the X-ray centre candidate which will be discussed later in this section.

From our findings, all definitions give similar signals. We note that, for the X-ray centre definition, the signal is slightly higher and the SIS fitting has smaller uncertainties compared to the two other candidates. Therefore, our results suggest that the X-ray centre is better at tracing the centre of mass. In contrast to our findings, the X-ray definition poorly traces the centre in George et al. (2012). From their signals, they argue that the most massive galaxy is better at tracing the centre of mass halos than the WC and the X-ray centre for their groups. We suspect the large uncertainties in the centroid candidate positions (WC and X-ray centre definitions) from George et al. to be a potential cause of this contradiction.

The weighted centre in George et al. may not be as well defined as in the GEEC catalog. This stems from the fact that, contrary to the GEEC catalog, the COSMOS group catalog survey did not benefit from a high redshift completeness (only 20% of the group members have spectroscopic redshifts (George et al., 2011)). Therefore, the member galaxies were selected from a membership probability based on the available photometric redshifts. Consequently, the probability of contamination due to interloper or projection effect is higher in the COSMOS group catalog.

The X-ray groups from GEEC catalog as well as in the COSMOS catalog were both selected from *XMM-Newton* and *Chandra* data following the same procedure outlined in Finoguenov et al. (2007). The uncertainty in the X-ray centre in the GEEC group catalog is of order of 10", but it can reach 30" for systems of low statistical significance. For the COSMOS catalog, the X-ray position uncertainty is 32" for groups with ambiguous spectroscopic association and, 32" divided by the significance for groups with confident spectroscopic association. The mean uncertainty in the X-ray centroid position is 23" (George et al., 2011). Therefore, the offsets for the WC and X-ray centre definition in George et al. can be due to the large uncertainties in their location.

One important thing to point out is that galaxy shape measurements in the COSMOS field were done with high-resolution imagery from the Hubble Space Telescope which allows the detection of fainter sources. This advantage provides smaller uncertainty on their signal and therefore gives access to an extra bin at small radii which is not available in our measurements due to signal to noise constraints. At such radii, George et al. consider the possibility of an offset in the lensing signal caused by the contribution of the halo mass around the MMG candidate. They tested this theory by using a Markov chain Monte Carlo method and their best fitting shows that there are no detectable halos around the MMG.

From the construction of mock group catalogues based on the large SDSS galaxy groups catalogues, Skibba et al. (2011) compute and compare the cumulative distribution of the line-of-sight velocity and projected position offsets. From statistical analysis, they show that the SDSS and the mock catalog without any offset are not drawn from the same distribution suggesting that the brightest galaxy is not the central galaxy but instead a satellite galaxy. If this hypothesis is right and if the brightest group galaxy and the most massive galaxy are the same object (which is true more than 90% of the time in the SDSS and the GEEC samples), then one would not expect the weak lensing signal to be maximized at small radii around the MMG. Our results are consistent with the Skibba et al. findings, as we find that the WC and X-ray are better at tracing the centre of mass than the MMG especially around optical groups, while all definitions work equally well for X-ray groups.

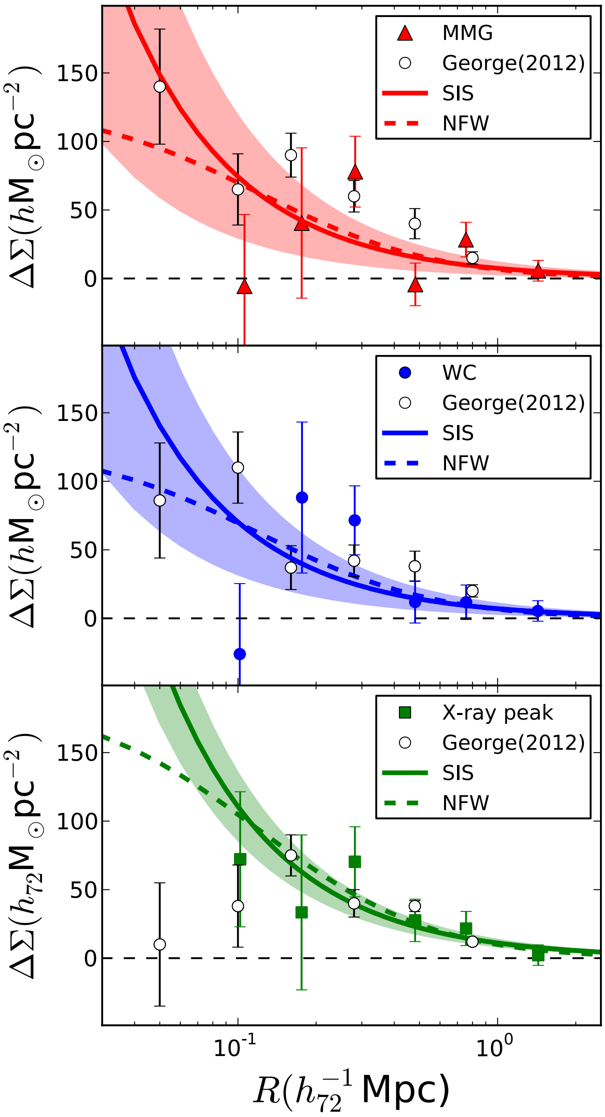

Figure 5.1: Stacked weak lensing signal using the MMG definition (top panel), the WC definition (middle panel) and the X-ray centre definition (bottom panel). The red triangles, blue circles and green squares are measured from our sample while the black open circles are measured from COSMOS group catalog by George et al.(2012). The fitting legend on our sample is the same as in Figure 4.2. The error bars represent the statistical uncertainty.

5.2 Summary

Locating the centre of galaxy groups is important, although it remains observationally very challenging. Weak lensing, strong lensing and dynamical methods constitute complementary techniques to test the validity of different tracers of group centres. In this work, we used the weak lensing and dynamical methods to test two different centre definitions: WC and MMG. In addition, for the X-ray groups we can use the X-ray peak as a third centre definition. We detected a significant weak lensing signal for a complete sample of 85 groups from the GEEC catalog at redshifts 0.1< z <0.9. Additionally, we present the lensing signal stacked around X-ray and optically selected groups separately. Finally, the influence of unrelaxed groups on the weak lensing signal for X-ray and optical groups has been analyzed for the first time where these unrelaxed groups were detected using the AD and DS tests in Connelly et al. (2012). We compare our findings with George et al. (2012) who used galaxy groups from the COSMOS survey. Furthermore, we evaluate the VDP for the entire sample using the WC and MMG definitions. However, the uncertainties in our profiles from this technique are too large to clearly discriminate which centre definition is the best at tracing the potential well in groups. The main conclusions of this thesis are:

1. The lensing signal for the entire sample reaches higher values when using the WC definition than when using the MMG. Therefore, our findings indicate that the MMG is not the best definition of centre in groups. This first result is not in agreement with the findings in George et al. which concludes that the MMG is better at tracing the centre of mass than the WC and the X-ray centre. Nevertheless, our results are roughly consistent with Skibba et al. which argue that the BHG is generally not the central galaxy.

2. By splitting the sample into two subsets, optically selected and X-ray selected galaxy groups, we come to the conclusion that all definitions of centre work well for the X-ray selected sample, with a preference for the X-ray centre definition. For the optically selected groups, the WC is a significantly better definition of the centre than the MMG.

3. Once we removed groups classified as dynamically complex, the weak lensing signals of the MMG, WC and X-ray centre definitions are in better agreement.

4. The lensing profiles and lensing signals, when restricting our sample to X-ray groups, are consistent with George et al. (2012) on the scales where our measurements overlap. We conclude that higher imaging resolution is required in order to confirm if the inner profiles are in agreement.

5. From the VDP, the MMG definition is slightly favoured over the WC with uncertainties too large to confirm. More satellites needs to be added to the sample in order to decrease the uncertainty.

Despite the fact that our group sample is very well-defined, it is modest in size. Having a much larger sample of groups with very high completeness would improve the constraints on the density profiles of dark matter halos and would allow a better understanding of groups with large offset between the most massive galaxy and the halo centre. Moreover, the poor statistics in the dynamical method do not allow us to constrain differences in centre definitions.

In future work, we would like to analyze group centres on much larger samples and improve the completeness of our data. Prospective samples such as the SDSS and zCOSMOS group catalogs would significantly enlarge the sample size. The gain of HST imaging with extra spectroscopic observations would improve the membership and source completeness and therefore provide the opportunity to trace the weak lensing and the surface density at smaller radii. Eventually, we would like to evaluate the VDPs around different centre definitions on groups provided from simulations such as Millennium Simulation and compare if these VDPs are consistent with observations.

Bibliography

Connelly, J. L., Wilman, D. J., Finoguenov, A., et al. 2012, ApJ, 756, 139

Finoguenov, A., Guzzo, L., Hasinger, G., et al. 2007, ApJS, 172, 182

Finoguenov, A., Connelly, J. L., Parker, L. C., et al. 2009, ApJ, 704, 564

George, M. R., Leauthaud, A., Bundy, K., et al. 2011, ApJ, 742, 125

George, M. R., Leauthaud, A., Bundy, K., et al. 2012, ApJ, 757, 2

Skibba, R. A., van den Bosch, F. C., Yang, X., et al. 2011, MNRAS, 410, 417